EFDA–JET–PR(11)61

P.A. Schneider, E. Wolfrum, R.J. Groebner, T.H. Osborne, M.N.A. Beurskens,
M.G. Dunne, J.R. Ferron, S. Günter, B. Kurzan, K. Lackner, P.B. Snyder,
H. Zohm, the ASDEX Upgrade Team, the DIII-D Team
and JET EFDA contributors

Differences in the H-mode Pedestal Width of Temperature and Density

Differences in the H-mode Pedestal Width of Temperature and Density

P.A. Schneider[1], E. Wolfrum[1], R.J. Groebner[2], T.H. Osborne[2], M.N.A. Beurskens[3], M.G. Dunne[4], J.R. Ferron[2], S. Günter[1], B. Kurzan[1], K. Lackner[1], P.B. Snyder[2], H. Zohm[1], the ASDEX Upgrade Team[1], the DIII-D Team2 and JET EFDA contributors*

JET-EFDA, Culham Science Centre, OX14 3DB, Abingdon, UK

1 Max-Planck-Institut für Plasmaphysik, EURATOM Association, Garching, Germany
[2]General Atomics, PO Box 85608, San Diego, CA 92186-5608, USA
[3]URATOM-CCFE Fusion Association, Culham Science Centre, OX14 3DB, Abingdon, OXON, UK
[4]Department of Physics, University College Cork, Association Euratom-DCU, Cork, Ireland
** See annex of F. Romanelli et al, "Overview of JET Results",*
(23rd IAEA Fusion Energy Conference, Daejon, Republic of Korea (2010)).

Preprint of Paper to be submitted for publication in
Plasma Physics and Controlled Fusion

Abstract

A pedestal database was built using data from type-I ELMy H-modes of ASDEX Upgrade, DIII-D and JET. ELM synchronized pedestal data was analysed with the two-line method. The two-line method is a bilinear fit which shows better reproducibility of pedestal parameters than a modified hyperbolic tangent fit. This was tested with simulated and experimental data. The influence of the equilibrium reconstruction on pedestal parameters was investigated with sophisticated reconstructions from CLISTE and EFIT including edge kinetic profiles. No systematic deviation between the codes could be observed. The flux coordinate system is influenced by machine size, poloidal field and plasma shape. This will change the representation of the width in different coordinates, in particular, the two normalized coordinates Ψ_{N} and r/a show a very different dependence on the plasma shape.

The scalings derived for the pedestal width, Δ, of all machines suggest a different scaling for the electron temperature and the electron density. Both cases show similar dependence with machine size, poloidal magnetic field and pedestal electron temperature and density. The influence of ion temperature and toroidal magnetic field is different on each of $\Delta_{T\mathrm{e}}$ and $\Delta_{n\mathrm{e}}$. In dimensionless form the density pedestal width in Ψ_{N} scales with $\rho_{\mathrm{i}\star}^{0.6}$, the temperature pedestal width with $\beta_{\mathrm{p,ped}}^{0.5}$. Both widths also show a strong correlation with the plasma shape. The shape dependence originates from the coordinate transformation and is not visible in real space. The presented scalings predict that in ITER the temperature pedestal will be appreciably wider than the density pedestal.

1. INTRODUCTION

The H-Mode regime in a fusion plasma was first observed in the ASDEX tokamak [1]. It is characterised by increased energy confinement and a remarkable edge region. At the plasma edge a pedestal in temperature and density is present. Over a few percent of the plasma radius, or several mm to a few cm, temperature and density gradients which are typically an order of magnitude higher than those elsewhere in the plasma can be sustained. Because of stiff core temperature profiles [2] a significant fraction of the plasma stored energy is sustained by the edge pedestal.

Investigations of the pedestal are challenging, not only because of the small spatial scales but also because of fast recurring edge localized modes (ELMs). Therefore, time resolutions on the millisecond scale are necessary. Diagnostics are constantly improved in order to resolve the pedestal in more detail. However, the uncertainties inherent in measuring the gradient and width of the pedestal remain relatively high, especially when considering the variation of gradients and widths which can be achieved in a single machine. The limitations in machine operation seldom allow variations of key quantities (poloidal and toroidal magnetic field, pedestal temperature and density) over more than a factor of two and allow no variation in machine size. However, a large variation in parameters is required to verify trends predicted by theory or to empirically scale to future fusion devices.

Analysis techniques and multi-machine comparisons are therefore important. The analysis must be optimised to minimise additional uncertainties aside from diagnostic limits. Comparisons between different machines allow broadening of the available parameter space. The present paper focuses on a comparison between the three tokamaks ASDEX Upgrade (AUG), DIII-D and JET. The three machines have a different size and cover a wide range of plasma current, magnetic field, plasma pressure and shape. The range in these parameters and those used in the paper is listed Tab. 1. All analyses are performed with this set of data if not stated otherwise. The same analysis code was applied to data of each device. This minimizes systematical uncertainties which may arise from different data treatment.

In the recent years a lot of effort was put into precise measurements of the pedestal width with the goal to understand the mechanism setting the width [3, 4, 5, 6, 7, 8]. Main mechanisms in the discussion are turbulence suppression due to different flow shear mechanisms [9, 10], the atomic physics of neutral penetration in the pedestal [11, 12] and MHD effects like the kinetic-ballooning modes [13]. Besides their different dependencies on plasma parameters also the radial coordinates are important for the pedestal width. For example, do MHD physics act in normalized flux while real space coordinates are relevant for neutral penetration. Therefore, it is important to understand the differences in the coordinate systems and how the coordinate transformations are influenced by the parameters relevant for pedestal physics.

The paper is structured in four sections. In the first section the diagnostics and temporal and spatial data selection is introduced, then 3 different methods to characterise the pedestal are presented and benchmarked against a set of randomly generated data. The second section focuses on the different coordinate systems and how they depend on various plasma parameters. This is combined with a crosscheck between the equilibrium codes CLISTE and EFIT. The third section is concerned with the identification of the separatrix position with only the use of profiles of temperature and density. In the fourth section measurements of the pedestal width on the three devices are described in two different ways, first with dimensionless physics quantities and second with engineering parameters. The paper closes with a summary and outlook.

2. METHODS

The profile analysis is done with composite ELM synchronized profiles. Data is accumulated and ELM synchronized over an interval of 0.1-1.0 s in a globally stationary plasma. Only measurements immediately before the onset of an ELM are selected and compiled into a single pseudo profile.
During ELMs the current flowing onto the divertor is strongly increased. In AUG this current is measured with shunts and indicates the onset of an ELM [14]. The relevant period for profile synchronisation is defined from -3.5 ms to -1.5 ms relative to the ELM onset time, but at least 4 ms after the previous ELM. In this interval the pedestal pressure is not influenced by the ELM instability any more [15]. In DIII-D and JET D_α radiation peaking in the divertor region is used to determine the ELM onset. ELM synchronized profiles are composed of the last 20% of the ELM cycle. Further improvement of the spatial coverage is achieved by a radial sweep of 1.5-4 cm of the whole plasma column. This shift creates virtual lines of sight. The higher spatial coverage is especially important to determine gradients with high accuracy.
At AUG the diagnostics for the electron temperature pedestal are the electron cyclotron emission (ECE) [16] and the vertical Thomson scattering (VTS) [17]. The electron density pedestal is measured with Interferometry [18], Li-Beam [19, 20, 21] and VTS. The combination of multiple diagnostics is necessary because the VTS generally measures only inwards to about 2/3 of the pedestal top. The ECE is also often not able to measure the whole pedestal. In type-I ELMy H-mode the plasma is optically thin in the whole SOL and about 1/3 of the pedestal. In this case the assumption of black body radiation used in the evaluation of the temperature is not correct. This effect is generally referred to as shine through [22]. The uncertainty of the electron density at the pedestal top is reduced by combining Li-Beam measurement with results from interferometry [23]. The Thomson scattering measures T_e and n_e at the same position in the plasma and allows for the correction of mapping errors. This correction is essential to determine the electron pressure. This is discussed in more detail in Sections 3 and 4. At DIII-D and JET the Thomson scattering diagnostics [24, 25] are set up differently than in AUG and it is possible to analyse the whole pedestal. Therefore, no uncertainties can be introduced by the alignment of different diagnostics. However, the temporal resolution is generally lower and the time interval for the composite profiles necessarily increases. In the case of JET the large size of the scattering volumes was taken into account. This was done with a Richardson-Lucy-Deconvolution [26] using the approximation found in [27].
The composite pedestal profiles are characterised by their top value, bottom or separatrix value, width and gradient. For comparison with theory it is essential to determine the pedestal parameters consistently for a large variety of global plasma parameters. Considering the finite resolution of the diagnostics it is convenient to characterize the pedestal with a functional form. The most common functional form is a modified hyperbolic tangent function (mtanh). The mtanh consists of a hyperbolic tangent in the pedestal and is supplemented with two polynomials, one for the core and one for the SOL (see e.g. [28]). Two other approaches, the two-line method and low pass filtering, are introduced in the next sections. The advantages and disadvantages of these methods are discussed.

2.1. TWO-LINE METHOD

In type-I ELMy H-mode the edge profile (last 20% of the radius in Ψ_N) exhibits two pronounced changes in the gradient. This divides the edge into three regions: the edge of the core plasma, the pedestal and the SOL. In the SOL parallel transport is dominating and inside of the separatrix a transport barrier forms due to reduced transport [29]. When the SOL is excluded from the analysis, the pedestal top separates the two remaining regions. The pedestal and the

edge of the core plasma have distinct gradients. These gradients can be approximated with constants within the experimental uncertainties. Considering this shape of the pedestal it is convenient to define the function

$$f(x) = \begin{cases} a_2(a_0 - x) + a_1 \text{ for } x \leq a_0 \\ a_3(x - a_0) + a_1 \text{ for } x > a_0 \end{cases} \quad (1)$$

where a_n are free parameters. A fit of the plasma edge from $\rho_\mathrm{p} \sim 0.88$ up to the separatrix immediately yields the pedestal top position a_0, the pedestal top value a_1 and the mean gradient over the pedestal a_3. The width of the pedestal Δ is then $x_\mathrm{sep} - a_0$. The determination of the separatrix position x_sep is discussed in Section 4 and is a source of uncertainties like the fit parameters. A typical application of Eq. (1) is illustrated in Figure 1. This method is similar to the one used at JT-60U [30] but with a different definition for the width. At JT-60U the pedestal width was defined as a_1/a_3.

2.2. LOW-PASS FILTER

All methods to determine the pedestal parameters use specific features in the profile shape. Extrema in curvature are the most pronounced features of the pedestal profile. However, the scatter in the experimental data prevents direct determination of the profile curvature. Fitting the data with various functional forms helps to determine the profile shape. A different approach is to smooth the scattered data.

One possibility to smooth the data is to apply a low-pass filter. If the radial coordinate is interpreted as temporal coordinate the radially distributed data becomes a frequency signal. The scatter in the data corresponds to a high frequency component. The relevant low frequency component can be extracted in frequency space with a low-pass filter. An example with a Butterworth frequency filter is shown in Fig. 2. Topmost in Fig. 2.1 density data from the Li-Beam diagnostic is shown with a smoothed curve for the pedestal region in AUG. Below the density profile the gradient and curvature are illustrated as derived from the smoothed density pedestal, the vertical lines indicate pronounced features in the pedestal structure. Fig. 2.2 shows the smoothing kernel for this example, the FWHM of the central maximum is about 1.4 cm. The correct choice of this width is essential for useful curvature values. The curvature is declared as useful when it defines a clear pedestal top and pedestal bottom. The advantage of frequency filtering is an optimal balance between a smooth curve and preserving the pedestal structure. In comparison, smoothing with a Gaussian kernel would not satisfy both needs. The information about gradients would be lost when optimising the kernel width for well defined curvature values. The pedestal top is defined as the point of extremal curvature which is located inside of the maximal gradient. The pedestal bottom also has extremal curvature but lies outside of the maximal gradient.

The low-pass filter method does not include uncertainties of individual data points. The scatter in the data must represent the uncertainties. Therefore, the low-pass filter method is more sensitive to outliers than least squares fitting which accounts for larger uncertainties of single data points. Without special treatment for outliers the resulting pedestal parameters will be wrong. For a Thomson Scattering measurement with individual uncertainties this means to set an upper threshold for the uncertainty which reduces the number of outliers. The filter method inherits no shape restriction like the mtanh or two-line method. On the one hand, this will lead to large uncertainties when the data has a low spatial resolution. On the other hand, local parameters like the maximal gradient will be more accurate as separated regions in the edge do not influence each other. However, this is only true if the kernel width was chosen correctly. Therefore, the filter method is not adequate as a stand alone technique to analyse the pedestal. But in combination with the kernel width provided by mtanh or two-line method it can provide

supplementary information about the pedestal structure. Using the advantages of more than one method improves the results of the analysis.

2.3. BENCHMARKING OF METHODS

For the discussion of the results it is important to document the properties of the different methods to characterize the edge pedestal. Two tests were performed to assess these properties. First, the methods were applied to simulated data with known pedestal parameters and asymmetric profile shape. Second, real data was analysed for similar discharges where the pedestal parameters are expected to be unchanged.
The simulated pedestals consist of three regions with different gradients and continuous transitions between them. The artificial data points are distributed normally around this curve. The standard deviation of the data points is 7% in vertical and 2 mm in radial direction. These values are chosen to resemble optimal measurements at AUG. An examplary artificial pedestal profile is illustrated in Fig. 3. A simulation consists of 500 profiles with the same properties but randomly scattered data points. The different simulations are selected to test and document the influences of assymetries in the pedestal. The parameters of each pedestal - top, width, gradient - are determined with the different methods. This gives a single mean value with a certain standard deviation for each simulation, method and pedestal parameter. In Fig. 4 the results of three tests are shown for the three methods. For each pedestal parameter the relative deviation from the set value is illustrated. The set value is of no real importance since it was arbitrarily chosen to match the definition of the two-line method. Therefore, a constant offset only illustrates the differences with the two-line method. Of interest are the variations of one method within a group of simulations where one or more of the set values are fixed. In the first column the pedestal itself is unchanged, only the core gradient is varied. A temperature profile is generally more peaked than the density profile. Therefore, a core gradient in arbitrary units of $1-5$ would correspond to a density like profile and $6-12$ to a temperature or pressure like profile. The filter and two-line method are not influenced by the change of the core gradient. The mtanh method reproduces the pedestal width accurately. However, it shows a clear change of about 20% in pedestal top and gradient, although, these parameters were the same in all cases. This is likely a result of the point symmetry of the hyperbolic tangent function. Because of its symmetry the mtanh's ability to fit asymmetric profiles is diminished. Although, the additional polynomials in the mtanh should cope with assymetries, they do not resolve the problem completely. A second test is shown in the middle column of Fig. 4. Again the pedestal width is kept constant but the pedestal top value and consequently the pedestal gradient is varied. Filter and two-line method yield constant width and can follow the variation in the pedestal top. The mtanh method reproduces the pedestal parameters well unless the ratio of pedestal gradient and core gradients becomes small. This is visible when the low pedestal top values (small pedestal gradients) are compared to the large pedestal top values. The mtanh gives a 25% difference for the width, although, the width was not varied in the parameter scan. In the third column pedestal width and gradient were varied. Pedestal top and core gradient were set to values where all three methods showed good results before. The pedestal parameters determined with two-line and mtanh are in good agreement with each other for widths larger than 1.5 cm. The large relative deviation for the case with 1.0 cm pedestal width is due to the finite radial resolution in the simulation. The simulation covered a variety of different possible pedestal shapes and the two-line and mtanh methods were found to agree within 10% for most cases. The radial scatter of the data points in the simulation was normally distributed with a standard deviation of 2 mm. This scatter is represented by the error bars of pedestal width and gradient in Fig. 4. In this case the pedestal width cannot be determined to better than ± 3 mm. In real measurements the conditions are not so predefined as in a simulation. In order to get

useful statistics an AUG standard scenario with plasma current 1 MA, toroidal field 2.5 T, heating power 6 MW and gas puffing $1.2 \cdot 10^{22}\mathrm{s}^{-1}$ was chosen to compare the two-line and the mtanh method. The pedestal width determined with the two-line method depends on the pedestal top and the separatrix position. The separatrix position has to be determined separately as described in Section 4. The mtanh method directly gives the pedestal width as width of the modified hyperbolic tangent function. For this series of over 50 independent time slices in different discharges reproducible pedestal parameters are expected. These profiles were analysed with both methods. The mtanh model yielded a mean width $\Delta_{n\mathrm{e}} = 1.8$ cm with a standard deviation of 0.8 cm, a pedestal top density $n_{\mathrm{e,ped}} = 7.6 \pm 0.9 \cdot 10^{19}$ m^{-3}, a temperature pedestal width $\Delta_{T\mathrm{e}} = 1.9 \pm 0.5$ cm and $T_{\mathrm{e,ped}} = 0.38 \pm 0.09$ keV. The results for the two-line method were $\Delta_{n\mathrm{e}} = 1.7 \pm 0.2$ cm, $n_{\mathrm{e,ped}} = 6.9 \pm 0.5 \cdot 10^{19}$ m^{-3}, $\Delta_{T\mathrm{e}} = 1.7 \pm 0.3$ cm and $T_{\mathrm{e,ped}} = 0.43 \pm 0.03$ keV. Within the uncertainties both methods result in the same pedestal parameters. However, the two-line method shows significantly reduced scatter.
To summarize, in a simulation data points were statistically distributed around a known curve. The distribution was normal and inherited no systematic effects. The mtanh method was reliable over a wide range of parameters. However, the mtanh was also subject to its symmetry and yielded systematic deviations. This was visible when the pedestal parameters were constant and only the symmetry of the profile was varied. The two-line method was not influenced by the symmetry as expected. Although, the uncertainty compared to the mtanh is increased due to the additional need to determine the separatrix position, a large set of identical AUG discharges showed reduced scatter in the pedestal parameters of the two-line method compared to the mtanh method. This suggests abandoning a physical shape allows the two-line method to determine the basic characteristics of the pedestal with reduced scatter. This is beneficial for the analysis of large data sets. The mtanh method has clear advantages as experimental input for modelling or when additional information of the SOL is of interest. In the present work only the general characteristics of the pedestal are relevant. Therefore, the two-line method was used for the analysis in Section 5. The filter method is reliable only with a priori knowledge about the size of the pedestal. Therefore, it is not useful as standalone technique. However, it can be used supplementary to the other methods since it has no symmetry constraint as the mtanh and gives more information about gradients and curvature than the two-line method.

3. INFLUENCE OF THE EQUILIBRIUM RECONSTRUCTION

In tokamak geometry the reconstruction of the magnetic equilibrium plays an important role to combine measurements from different locations in a tokamak. Different boundary conditions in the equilibrium reconstruction influence the mapping of measurement locations. This can lead to deviations in the pedestal width and pedestal gradients. In this section these effects are investigated with CLISTE [31] and EFIT [32].
The measurements themselves are conducted in machine coordinates R, z, ϕ with radial coordinate R, vertical coordinate z and toroidal angle ϕ. These coordinates are determined for each diagnostic during calibration and are assumed to be without any uncertainty in the remainder of this section. Because of toroidal symmetry ϕ is dropped. In order to compare measurements from different locations it is convenient to map R, z to 1D normalized poloidal flux coordinates

$$\Psi_{\mathrm{N}} = \frac{\Psi - \Psi_{\mathrm{ax}}}{\Psi_{\mathrm{sep}} - \Psi_{\mathrm{ax}}}, \tag{2}$$

with the 2D flux function Ψ, the flux at the plasma center Ψ_{ax} and at the separatrix Ψ_{sep}. This can be done for all flux surfaces. In many cases it is helpful to consider profiles again in real space. Therefore, the Ψ_{N} coordinates are mapped back to R, z. For a definite relation in the inverse mapping, z is set to the value at the magnetic axis z_{mag}. The resulting real space coordinate is then called R_{maj}. Analogous to the R_{maj} coordinate, also an un-normalized 1D flux coordinate can be defined as Ψ_{maj}. At AUG another normalized coordinate $\rho_{\mathrm{p}} = \Psi_{\mathrm{N}}^{0.5}$ is often used. Analogous to poloidal flux coordinates, toroidal flux coordinates can also be defined, however, these are not used in this work, since toroidal flux is only defined up to the separatrix.
The equilibrium reconstruction is generally done with codes like CLISTE or EFIT, which mainly consist of a Grad-Shafranov solver and several constraints defined by theory and measurement. The amount of experimental constraints applied in the equilibrium reconstruction varies for different applications. The equilibria based only on magnetic measurements will be called generic equilibria, these are always available and are normally used for profile analysis. More sophisticated equilibria can also include kinetic profiles and fast particle simulations to constrain the total pressure [33, 34] and are called kinetic equilibria. Because their preparation is normally time consuming, these equilibria are generally only used as input for further calculations such as stability analyses. In this section the influence on profile analysis is quantified by applying generic and the more sophisticated kinetic equilibria.

3.1. DIFFERENCES DUE TO EXPERIMENTAL CONSTRAINTS

Generic and kinetic equilibria are compared for the same discharges in order to assess the influence of the boundary conditions on the pedestal width and gradient. The flux surface compression $\partial\Psi/\partial z$ or $\partial\Psi/\partial R$ is used to quantify differences in the reconstructions. The following analysis is based on nineteen pairs (generic and kinetic) of EFIT reconstructions for DIII-D discharges involving an edge safety factor q_{95}-scan from $4-7$ at high triangularity $\delta = 0.5$ and global poloidal beta $\beta_{\mathrm{p}} = 1-2$. Assuming the kinetic equilibria best resemble the reality, several uncertainties arise when using generic equilibria. The influence of normalizing the flux coordinates is illustrated in Fig. 5 for the flux surface compression $\partial\Psi_{\mathrm{N}}/\partial z$ along the Thomson Scattering chords of DIII-D. The combined $\partial\Psi_{\mathrm{N}}/\partial z$ is generated with the normalisation factor derived from the kinetic equilibrium and the generic flux compression $\partial\Psi/\partial z$. The difference between generic and combined flux compression is up to 10%, mainly due to different values of Ψ_{ax}. Besides the deviation in normalization this example shows the effect

of a different current profile. This difference is expected since the bootstrap current is taken into account only for the kinetic case. All EFIT reconstructions show a larger $\partial\Psi_{\mathrm{N}}/\partial z$ for the generic case. In regions where the bootstrap contribution is negligible $\partial\Psi_{\mathrm{N}}/\partial z$ deviates by 5-20%. In regions of significant bootstrap current the deviation increases to 10-30%. However, the difference in the reconstruction cannot be explained with deviations in normalization and current profiles alone. Also differences in Shafranov-Shift $\beta_{\mathrm{p}} - li/2$, safety factor q_{95} and plasma shape (δ, κ, R_{sep}) contribute to the deviation in $\partial\Psi_{\mathrm{N}}/\partial z$. Equilibrium reconstructions by CLISTE at AUG show similar behaviour as those done with EFIT at DIII-D. With CLISTE a power scan $6.5 - 13.5$ MW at constant q_{95} was analysed. The flux surface compression increases with heating power similarly for generic and kinetic reconstructions. However, the higher heating power results in larger edge pressure gradient and increased bootstrap contribution. This causes localised deviations in $\partial\Psi_{\mathrm{N}}/\partial R$ for generic and kinetic reconstructions which scale with the heating power. In Figure 6 the relative deviation in flux compression is plotted over the plasma edge. At low heating power deviations below 5% are observed while this increases to over 10% at higher heating power.
The equilibria for the analyses are all based on experimental measurements and cover a wide range of plasma parameters. However, the range was not sufficient to draw final conclusions about the mechanisms behind the observations. Therefore, a more sophisticated analysis should be conducted, with the goal to improve generic equilibrium reconstructions.
Concerning pedestal profile analysis the significance of the error introduced by the equilibrium reconstruction is assessed in the following. The error does not seem to depend systematically on global values like e.g. the Shafranov-Shift, but on the constraints in the equilibrium reconstructions. Especially, neglecting the bootstrap current leads to systematic deviations in the flux surface compression. The bootstrap current is also dependent on edge gradients [35]. The gradients themselves are determined with knowledge of the flux surface compression. This results in a systematic increase of the flux surface compression for generic equilibria, which influences the mapping of measurements from R, z to Ψ_{N}, Ψ_{maj} or R_{maj}. With an overestimated flux surface compression a pedestal profile appears to be broader in Ψ_{N} coordinates and shows smaller gradients. This is illustrated in Figure 7 where an arbitrary edge parameter is plotted against Ψ_{N}. Both profiles are identical in R, z coordinates, but they deviate after mapping to Ψ_{N} coordinates. The profile obtained with the generic reconstruction appears to be broader. Initially broader profiles experience a larger relative broadening. This is because the largest deviation in $\partial\Psi_{\mathrm{N}}/\partial z$ or $\partial\Psi_{\mathrm{N}}/\partial R$ extends farther inwards than a typical pedestal (see Figures 5, 6). The results for the equilibrium reconstruction with EFIT are summarized in Table 2. The deviations in the flux surface compression are comparable at different plasma positions - here the position of the DIII-D Thomson Scattering system and the outer midplane. Therefore, these errors cancel each other after the transformation to R_{maj} coordinates.
In summary, uncertainties due to equilibrium reconstruction are avoided when the analysis is performed in the real space coordinate system of the measurement. However, normalized flux coordinates might be important for the underlying physics (e.g. [13]) and therefore necessary for the analysis. The comparison between generic and magnetic equilibrium reconstructions showed that deviations of up to 30% in $\partial\Psi_{\mathrm{N}}/\partial z$ are possible for single measurements. On average the deviation of derived quantities like pedestal width and gradient remain 10% or lower. However, this deviation is dependent on the edge bootstrap current and the initial width of the profile.

3.2. TRENDS DUE TO EXPERIMENTAL CONDITIONS

A change in the plasma conditions will influence the result of equilibrium reconstructions. This section documents the influence of plasma parameters on coordinate system transforma-

tions. It is illustrated how different coordinate systems impact the multi machine comparison between ASDEX Upgrade, DIII-D and JET.
Within a single device the flux surface compression can be manipulated with different heating levels. Figure 8 illustrates how $\partial\Psi_{\mathrm{N}}/\partial R$ increases with heating power in AUG. This is observed for kinetic and generic equilibrium reconstructions alike. The agreement suggests that generic reconstructions are suitable for analysing general dependencies. However, some effects might be lost when using less constraints in the equilibrium calculations. The analysis in the remainder of this section is performed with generic equilibria.
At the midplane the poloidal flux surface compression becomes $\partial\Psi_{\mathrm{maj}}/\partial R = -RB_{\mathrm{p}}$. However, the local poloidal field is not easily accessible experimentally. At the pedestal $\partial\Psi_{\mathrm{maj}}/\partial R$ is fairly constant as shown in Figure 8.1 and can be regressed from AUG, DIII-D and JET

$$\frac{\partial\Psi_{\mathrm{maj}}}{\partial R} \simeq 12.0 R_{\mathrm{mag}}^{1.08\pm0.14} \langle B_{\mathrm{p}}\rangle^{1.01\pm0.05} \beta_{\mathrm{p,ped}}^{0.14\pm0.04}, \tag{3}$$

with $\partial\Psi_{\mathrm{maj}}/\partial R$ measured in Vs/m, the normalized pedestal top pressure $\beta_{\mathrm{p,ped}} = p_{\mathrm{ped}}/(\langle B_{\mathrm{p}}\rangle^2/2\mu_0)$, the radius of the magnetic axis R_{mag}, the flux surface averaged poloidal field $\langle B_{\mathrm{p}}\rangle = \mu_0 I_{\mathrm{p}}/l$ and $l \propto a$ the plasma circumference at the last closed flux surface where a is the minor radius of the plasma. In Figure 9.1 $\partial\Psi_{\mathrm{maj}}/\partial R$ is averaged over the last 10% of the plasma radius (Ψ_{N}) and plotted against the approximation of Eq. (3). The regression is in quite good agreement with the data. This result is strong evidence that there are no systematic deviations between the equilibrium reconstructions for the individual machines. This also illustrates the difference between the flux surface averaged poloidal field and its local value at the outer midplane. It becomes $B_{\mathrm{p}} \propto \langle B_{\mathrm{p}}\rangle \beta_{\mathrm{p,ped}}^{0.14}$ and therefore $\beta_{\mathrm{p,ped}} = \beta_{\mathrm{p,ped,local}}^{0.72}$. This means the local poloidal field is roughly 25% larger than the flux surface averaged field.
The compression of normalized flux in real space can be divided into two components by using the definition of the normalized flux in Equation (2)

$$\frac{\partial\Psi_{\mathrm{N}}}{\partial R} = \frac{1}{\Psi_{\mathrm{sep}} - \Psi_{\mathrm{ax}}} \frac{\partial\Psi}{\partial R}, \tag{4}$$

where $\Psi_{\mathrm{sep}} - \Psi_{ax}$ is the normalization factor. For a cylindrical plasma the normalisation factor becomes $\Psi_{\mathrm{sep}} - \Psi_{\mathrm{ax}} \propto \mu_0 I_{\mathrm{p}} a$ with the total plasma current I_{p}. If we neglect the pressure and approximate $B_{\mathrm{p}} \sim \langle B_{\mathrm{p}}\rangle$ the dependence on the plasma current drops and only a machine size dependence remains

$$\frac{\partial\Psi_{\mathrm{N}}}{\partial R} \propto \frac{1}{a}\frac{1+\epsilon}{\epsilon}, \tag{5}$$

where $\epsilon = a/R_0$ is the inverse aspect ratio. The estimations which led to Eq. (5) neglect the real shape of the plasma and the local poloidal field. Still, for the machine comparison with AUG, DIII-D and JET a very similar scaling arises when including a shape factor. The machine size dependence is also found to be inverse but slightly less than linear.

$$\frac{\partial\Psi_{\mathrm{N}}}{\partial R} \simeq 1.65 a^{-0.70\pm0.05} \left(\frac{q_{95}}{q_{cyl}}\right)^{1.07\pm0.10}, \tag{6}$$

where $q_{cyl} = (2\pi a^2 B_{\mathrm{t0}})/(R I_{\mathrm{p}} \mu_0)(1+\kappa^2)/2$ is the cylindrical approximation of the safety factor, κ the plasma elongation and q_{95} the value of the safety factor at $\Psi_{\mathrm{N}} = 0.95$. The aspect ratio dependence in Eq. (5) could not be reproduced since there is no variation in ϵ for the available database. The quality of the approximation Eq. (6) is illustrated in Figure 9.2 and shows reasonable agreement for all three machines. In this representation the shaping factor $f_{\mathrm{q}} = q_{95}/q_{cyl}$ was introduced instead of $\beta_{\mathrm{p,ped}}$ because it is the better to describe the problem. With the regression parameters a and $\beta_{\mathrm{p,ped}}$ the RMSE increases by 50%. When applying the

regression to all three parameters a, f_{q} and $\beta_{\mathrm{p,ped}}$ Eq. (6) is not changed but the exponent of $\beta_{\mathrm{p,ped}}^{b}$ is found to be $b < 0.03$. This suggests f_{q} and $\beta_{\mathrm{p,ped}}$ together hold more information than a single quantity. This is not obvious because both quantities are strongly correlated in 0th order. In Figure 10 f_{q} strongly increases with $\beta_{\mathrm{p,ped}}$. However, there are also distinct trends visible for the different machines which could explain that f_{q} and $\beta_{\mathrm{p,ped}}$ are not interchangeable.

Applying a coordinate transformation - e.g. from real space to normalized flux space ($\partial\Psi_{\mathrm{N}}/\partial R$) - will influence all comparisons of widths and gradients. This coordinate transformation is dependent on machine size, aspect ratio, magnetic field, shaping and plasma pressure. All these parameters are also possible candidates in determining the pedestal width. In particular, following Eq. (6),the two dimensionless descriptions of the width flux space $\Delta_{\Psi_{\mathrm{N}}}$ and in real space Δ_{m}/a are not equivalent and will result in different scalings with q_{95}/q_{cyl} or $\beta_{\mathrm{p,ped}}$. For multi-machine comparisons it is important to use the correct coordinate system which is set by the underlying physics. For example normalized flux coordinates for MHD related physics and real space coordinates when atomic processes dominate the plasma edge.

4. SEPARATRIX POSITION

Measuring profiles of a single plasma parameter with different diagnostics may result in profiles which are misaligned with respect to each other after mapping in a 3D machine to 1D flux coordinates. Assuming the toroidal symmetry is unbroken this cannot be real and therefore must be an artifact of the spatial calibration or the mapping procedure. For different plasma parameters a radial misalignment between diagnostics is not as easily detected. However, proper alignment of different measurements is prerequisite for calculating dependent quantities. For pedestal studies positions based on the equilibrium reconstruction are not reliable enough. However, the separatrix as a prominent feature at the pedestal edge can be used to align different diagnostics. The separatrix position is also essential to determine the pedestal width with the two-line method.

Strategies to determine the separatrix position individually for temperature and density profiles use theoretical predictions for T_e and n_e at the separatrix based on divertor measurements and transport parallel to the field lines [36, 37]. A temperature of around 100 ± 20 eV at the separatrix is predicted for devices like AUG or DIII-D and 135 ± 30eV for JET. The temperature at the separatrix is only very weakly dependent on plasma parameters like heating power. The density can also be determined with this method, however, the uncertainty is larger and the value is not independent of gas fuelling. Fuelling has three major contributions: the regularly used gas puffing, neutral beam heating and recycling from the walls. Recycling strongly depends on the machine condition and previous discharges. Therefore, the exact gas fuelling rate cannot be determined precisely.

Another possibility to determine the separatrix position is a variation in the profile shape. Outside of the separatrix the field lines are not closed anymore and the large parallel transport becomes important [29]. When the particle transport is dominated by diffusion the gradients should have a discontinuity at the separatrix [36]. A similar discontinuity in the density gradient is predicted by a semi-analytical neutral penetration model for the plasma edge when the transport changes at the transition from closed to open field lines and should be independent of the gas fuelling [12]. In this section the position where the gradients change most is compared with the separatrix determined with the temperature measurement. The largest change of the gradients is associated with a maximum in the curvature.

The Thomson scattering (TS) system is used to evaluate the accuracy of a definition for the separatrix using only the n_e profile shape. TS is able to measure T_e and n_e simultaneously at the same location. Therefore, a comparison of T_e and n_e profiles with TS is not influenced by mapping uncertainties. The radial location of the 100eV-line is compared to unique features of the n_e profile. The instrument kernel of the TS system is around 6 mm at DIII-D and 3 mm for AUG. Therefore, a sharp kink in the gradient as expected from theory cannot be resolved experimentally. Consequently the point of maximal curvature in the density $\max(\nabla^2 n_\mathrm{e})$ is determined. This position is compared to the point of maximal gradient $\max(\nabla n_\mathrm{e})$ which should lie inside of the separatrix. These profile features are determined with the low-pass filter method described in Section 2.2. In the case of AUG the effective uncertainty increases a bit due to the mapping procedure. The uncertainty arising in determining the gradients is assumed to be normally distributed. The distributions $R_\mathrm{maj}(100\mathrm{eV}) - R_\mathrm{maj}(\max(\nabla n_\mathrm{e}))$ and $R_\mathrm{maj}(100\mathrm{eV}) - R_\mathrm{maj}(\max(\nabla^2 n_\mathrm{e}))$ then give information about the relative position of density profile features with respect to the separatrix determined via the temperature profile. In Figure 11 this is illustrated in a histogram. The relative frequency of discharges lying in a 3 mm bin is plotted. For DIII-D the distribution of the maximal curvature is peaked around -1 mm indicating a good match with the 100 eV position from T_e. The distribution of $R_\mathrm{maj}(100\mathrm{eV}) - R_\mathrm{maj}(\max(\nabla n_\mathrm{e}))$ is peaked around 5 mm showing that the point of maximal gradient is well inside the separatrix. In the case of AUG the TS is never available for

the whole pedestal. Therefore, the profiles consist largely of ECE and Li-Beam measurements. Due to their different locations these diagnostics are influenced by systematic misalignment due to the mapping. This becomes visible in Figure 11.2 where the distribution of $R_{\text{maj}}(100\text{eV}) - R_{\text{maj}}(\max(\nabla^2 n_{\text{e}}))$ peaks at -4.5 mm. With additional information of the TS system the average misalignment of ECE and Li-Beam was measured to be around 3 mm. When including this diagnostic shift the distribution of the maximal curvature of the density profile also peaks around -1 mm relative to the separatrix.

For the present data set of AUG and DIII-D discharges the position of maximal curvature of the n_{e} profile lies 1 mm outside of the separatrix determined via the 100 eV position of T_{e}. Regarding the FWHM of the distribution the uncertainty of this positioning is ± 3 mm. The absolute position of $T_{\text{e}} = 100$ eV can also not be determined more accurately than 3 mm. Therefore, the positioning of the separatrix is comparably accurate for the two presented methods, namely the 100 eV (135 eV for JET) position for T_{e} and the $\max(\nabla^2 n_{\text{e}})$. These are convenient methods to determine the pedestal width in T_{e} and n_{e} without including uncertainties in the separatrix position from equilibrium reconstruction (several mm to few cm) and uncertainties by mapping different diagnostics to the same 1D coordinates (few mm).

In the investigated data set no systematic dependencies of the positions on gas fuelling, heating power, shaping or collisionality were found within the spread of 6 mm. However, such dependencies cannot be excluded completely. Because a variety of different discharges was included in the analysis some effects might cancel each other. In a similarity experiment a dependence between the relative position $R_{\text{maj}}(\max(\nabla T_{\text{e}})) - R_{\text{maj}}(\max(\nabla n_{\text{e}}))$ and the pedestal density was observed [8]. Especially, the plasma shape and normalized pressure $\beta_{\text{p,ped}}$ were kept fairly constant. This is different to the data set applied here, which was selected to maximise the variation in shape and $\beta_{\text{p,ped}}$.

5. PEDESTAL WIDTH

The pedestal width in AUG and DIII-D was reported as being correlated with the square root of the poloidal pedestal beta $\beta_{\mathrm{p,ped}}^{0.5} \propto p_{\mathrm{ped}}^{0.5}\langle B_{\mathrm{p}}\rangle^{-1.0}$. This was observed in DIII-D for the electron pressure pedestal width for real space coordinates [3]. The mean pedestal width $(\Delta_{n\mathrm{e}} + \Delta_{T\mathrm{e}})/2$ was also found to scale with $\beta_{\mathrm{p,ped}}^{0.5}$ in normalized poloidal flux coordinates Ψ_{N} [13, 6]. For AUG the $\beta_{\mathrm{p,ped}}^{0.5}$ correlation could be reproduced for the electron and ion temperature but no dependence in the density pedestal width was found in ρ_{p} coordinates [7]. The mean pedestal width for AUG showed again a linear correlation with $\beta_{\mathrm{p,ped}}^{0.5}$ in Ψ_{N} but no correlation in real space [8]. The theory of kinetic ballooning modes predicts a $\beta_{\mathrm{p,ped}}^{0.5}$ dependence of the pedestal width in Ψ_{N} [38]. Besides the $\beta_{\mathrm{p,ped}}$ dependence of the pedestal width a $\rho_\star \propto T_{\mathrm{i}}^{0.5} M^{0.5} a^{-1} B_{\mathrm{t}}^{-1}$ dependence was also often discussed [3, 5, 6, 8], where M is the atomic mass number. However, both quantities have a similar dependency on the temperature and are difficult to distinguish. In [3] the temperature was varied while the total pressure was kept constant. The electron pressure width was found unchanged and therefore supports a $\beta_{\mathrm{p,ped}}$ dependence of the pressure width instead of a $\rho_\star$ dependence. In JT-60U also the mass number of the plasma's main ions was varied, the dependence of the ion temperature width on $\rho_\star^\xi$ was found to be less than $\xi = 0.2$ [5]. In DIII-D the variation of mass number was repeated to test a $\rho_\star$ dependence of the mean pedestal width in flux coordinates and no mass number dependence was found [6]. More recently a $\rho_\star$ test was performed with variation of machine size between DIII-D and JET [8]. The electron temperature and electron density pedestal width in real space r/a showed different correlations with $\rho_\star$. While $\Delta_{T\mathrm{e}}/a$ was uncorrelated with $\rho_\star$, $\Delta_{n\mathrm{e}}/a$ increased with $\rho_\star$. In theory of turbulence suppression via different mechanisms the pedestal width should scale with $\rho_\star$ to powers of 0.5-2.0 [10, 9, 39]. The density pedestal width in real space was found to scale with $1/n_{\mathrm{e}}$ for DIII-D [8] this is evidence for a role of neutral penetration in the pedestal [12].

The present study tries to pursue the progress in understanding the pedestal width physics. This is done by identifying the main parameters responsible for changes in the pedestal width of AUG, DIII-D and JET. The pedestal width is determined for all devices with the two-line method as described in Section 2.1. This study includes discharges from other studies [6, 7, 8] which are extended with new experiments from AUG including a current and triangularity scan. The main difference between this and previous studies is the database approach. In the studies listed above dedicated experiments were performed in order to study the influence of a single parameter on the pedestal. This was generally done in carefully designed similarity experiments or parameter scans. As a result precise information of one parameter was obtained. In consequence the information about other parameters and their correlation is not easily explored in these experiments. Especially, this is true for the plasma shaping which is generally matched in comparison experiments. It was shown in Section 3.2 that for the present data set the shaping factor q_{95}/q_{cyl} plays an important role and cannot simply be expressed in terms of normalized pressure. The database approach for analysing experiments might come at the expense of obscuring dependencies which do not appear statistically significant in the data set. Another uncertainty is included by influences on the plasma which are difficult to quantify like e.g. gas fuelling patterns, impurity content or radiation characteristics. Those influences can be reduced in dedicated experiments but not in a database approach.

This section searches for main contributors to the pedestal width in the given database. The consequences for theory are discussed in the conclusion. A special focus is put on the three independent plasma physics parameters normalized poloidal pedestal pressure $\beta_{\mathrm{p,ped}}$, normalized

toroidal gyroradius $\rho_{\mathrm{i}\star}$ and the normalized ion collisionality $\nu_{\mathrm{i}\star}$

$$\beta_{\mathrm{p,ped}} = 5.0265 \cdot 10^{-3} \frac{p_{\mathrm{e,ped}}[\mathrm{kPa}] + 1.602 \cdot T_{\mathrm{i,ped}}[\mathrm{keV}] n_{\mathrm{e,ped}}[10^{19}\ \mathrm{m}^{-3}]}{\langle B_{\mathrm{p}} \rangle^2 [\mathrm{T}]} \tag{7}$$

$$\rho_{\mathrm{i}\star} = 6.46 \cdot 10^{-3} \frac{T^{0.5}_{\mathrm{i,ped}}[\mathrm{keV}]}{a[\mathrm{m}] B_{\mathrm{t,ped}}[\mathrm{T}]} \tag{8}$$

$$\nu_{\mathrm{i}\star} = 4.90 \cdot 10^{-5} \frac{q_{95} R_0[\mathrm{m}] \ln\Lambda n_{\mathrm{e,ped}}[10^{19}\ \mathrm{m}^{-3}]}{\epsilon^{3/2} (T_{\mathrm{i,ped}}[\mathrm{keV}])^2}. \tag{9}$$

These equations are valid for a pure deuterium plasma and the values are calculated at the pedestal top in the electron temperature. The coulomb logarithm $\ln\Lambda$ is defined as $\ln\Lambda = 17.3 - 0.5\ln(n_{\mathrm{e}}[10^{20}\mathrm{m}^{-3}]) + 1.5\ln(T_{\mathrm{i}}[\mathrm{keV}])$. The assumption of a pure deuterium plasma is not the best in most cases. However, at AUG measurements of the average charge number Z_{eff} have a very large uncertainty at the plasma edge. This can be up to a factor of 2 and would obscure other influences in the database. Therefore, Z_{eff} is excluded from the analysis. For consistency the value of $Z_{\mathrm{eff}} = 1$ is used for all machines. For low collisionality $\nu_\star < 0.5$ the ratio of $T_{\mathrm{e}}/T_{\mathrm{i}}$ varied over a factor of 3 in DIII-D. At higher collisionality $T_{\mathrm{e}}/T_{\mathrm{i}}$ was rather constant, for AUG $T_{\mathrm{e}} \simeq 0.9 T_{\mathrm{i}}$ and for JET $T_{\mathrm{e}} \simeq 1.0 T_{\mathrm{i}}$. This assumption is used for Figure 12 when no T_{i} measurements are available from the edge CXRS, in the regression analysis only discharges with T_{i} measurements are included from AUG.

In Figure 12 the pedestal width of electron temperature and density is plotted against the single parameters $\beta^{0.5}_{\mathrm{p,ped}}$ (a),(b) and $\rho_{\mathrm{i}\star}$ (c),(d). In certain regimes both parameters show correlations with the pedestal widths. However, they alone cannot explain the pedestal width. Although, the pedestal width is best described with $\beta_{\mathrm{p,ped}}$ when using a single parameter, there is a systematic separation visible in (a),(b) towards larger $\beta_{\mathrm{p,ped}}$. This is not only true for the comparison between AUG and DIII-D data but also visible in the DIII-D data alone for $0.5 < \beta^{0.5}_{\mathrm{p,ped}} < 0.7$. A linear fit through the origin yields the coefficients 0.11 ± 0.02 ($\Delta_{T\mathrm{e}}$) and 0.11 ± 0.01 ($\Delta_{n\mathrm{e}}$) for $\beta^{0.5}_{\mathrm{p,ped}}$ for the AUG data alone. The uncertainty in the fit to density pedestal width is only small because of the boundary condition in the origin. For the temperature an offset linear fit with a slope of 0.13 would fit the data better. For DIII-D they become 0.088 ± 0.014 ($\Delta_{T\mathrm{e}}$) and 0.080 ± 0.015 ($\Delta_{n\mathrm{e}}$). The coefficients for DIII-D agree within the uncertainties with other studies which used the mtanh analysis method [40]. The differences between the machines cannot be explained by different analysis methods because the two-line method was applied in both cases. A linear fit for all machines would yield $\Delta_{T\mathrm{e}} \simeq (0.10 \pm 0.02)\beta^{0.5}_{\mathrm{p,ped}}$ with an RMSE of 21.0% and $\Delta_{n\mathrm{e}} \simeq (0.09 \pm 0.02)\beta^{0.5}_{\mathrm{p,ped}}$ with an RMSE of 22.5%. The plots with $\rho_{\mathrm{i}\star}$ Figure 12 (c),(d) show correlations between $\rho_{\mathrm{i}\star}$ and the pedestal width for certain regimes. However, $\rho_{\mathrm{i}\star}$ as single parameter is clearly not sufficient to describe the pedestal width. It has to be noted that $T_{\mathrm{e}} \neq T_{\mathrm{i}}$ for most DIII-D discharges and the gradients of T_{i} are smaller in the pedestal than those in T_{e}. For AUG at higher collisionality the gradients of T_{e} and T_{i} are typically similar. For DIII-D this suggests $\Delta_{T\mathrm{i}}$ should be larger than $\Delta_{T\mathrm{e}}$ while both widths are similar for the AUG discharges.

As this data is not from a single parameter scan also other influences can play a role. The most prominent influences were determined with a log-linear regression analysis. With special focus on the dimensionless parameters normalized pressure $\beta_{\mathrm{p,ped}}$, normalized gyroradius $\rho_\star$, collisionality $\nu_\star$, plasma elongation κ, q_{95}/q_{cyl} and $T_{\mathrm{e}}/T_{\mathrm{i}}$. In Figure 13 the pedestal width is plotted against a regression with all these parameters and with a subset of significant ones. Parameters are regarded as significant when their exponent is larger than 2σ. This criterion leads to two very different parameter sets. For the temperature pedestal width only pressure $\beta_{\mathrm{p,ped}}$ and plasma elongation κ appear significant. In the case of the density the normalized gyroradius $\rho_{\mathrm{i}\star}$, collisionality $\nu_{\mathrm{i}\star}$, q_{95}/q_{cyl} and κ show significant exponents. The temperature ratio

$T_\mathrm{e}/T_\mathrm{i}$ does not play an explicit role, however, it is implicitly included in the other quantities. With the significant parameters the scalings become

$$\Delta_{Te}[\Psi_\mathrm{N}] \simeq 0.42 \cdot \kappa^{-2.59\pm0.85} \beta_\mathrm{p,ped}^{0.51\pm0.09} \tag{10}$$

$$\Delta_{ne}[\Psi_\mathrm{N}] \simeq 2.90 \cdot \kappa^{-1.78\pm0.75} \rho_{\mathrm{i}\star}^{0.65\pm0.12} \nu_{\mathrm{i}\star}^{0.18\pm0.05} (q_{95}/q_\mathrm{cyl})^{1.45\pm0.29}. \tag{11}$$

The scaling to Δ_{Te} gives the same exponent for $\beta_\mathrm{p,ped}$ as it was used in the linear fits to the data. Adding the elongation improves the RMSE of the fit by 15% which is quite large considering the rather small available range $1.59 < \kappa < 1.88$. However, small width $\Delta_{Te} < 0.05$ are systematically overestimated by the scaling (Figure 13.3). For the density pedestal width the shape of the plasma influences the goodness significantly. Without κ the RMSE would increase by 15% and without q_{95}/q_cyl it would increase by 40%. This suggests an important role of the plasma shape in the pedestal formation. The triangularity δ is often used to describe effects of shaping. In the present database no correlation of the pedestal width with δ could be found. This suggests the triangularity might not be the best quantity to describe the shape in a multi machine comparison. The exponents of $\rho_{\star\mathrm{i}}$ and $\beta_\mathrm{p,ped}$ appear very similar in Eq. (11) and Eq. (10). Also in Figure 12 these parameters show similarities. Therefore, both parameters were exchanged for one another in the regression with the result that in all cases the quality of the fit was deteriorated. This would suggest that there are real differences in the pedestal width of T_e and n_e. This is further investigated with scalings to the factors of the dimensionless parameters. The factors are the four independent parameters machine size, magnetic field, temperature and density and they are extended with the elongation κ. The resulting regressions for the temperature and density width show already differences in the temperature dependence

$$\Delta_{Te}[\Psi_\mathrm{N}] = 0.025 \cdot a^{-0.56\pm0.28} \langle B_\mathrm{p} \rangle^{-0.93\pm0.20} T_\mathrm{e,ped}^{0.62\pm0.11} n_\mathrm{e,ped}^{0.54\pm0.15} \kappa^{-2.30\pm1.16} \tag{12}$$

$$\Delta_{ne}[\Psi_\mathrm{N}] = 0.011 \cdot a^{-0.67\pm0.19} \langle B_\mathrm{p} \rangle^{-1.01\pm0.22} T_\mathrm{e,ped}^{0.37\pm0.09} n_\mathrm{e,ped}^{0.51\pm0.15} \kappa^{-1.43\pm0.81}. \tag{13}$$

The fit quality can be improved by more than 10% with inclusion of the temperature ratio $T_\mathrm{e}/T_\mathrm{i}$ and the ratio between poloidal and toroidal field q_cyl which is significantly above the improvement expected for uncorrelated parameters. It is found that the temperature width is depending on the ion temperature and has no correlation with the toroidal field or q_cyl. The density width shows little correlation with the temperature ratio but depends on the magnetic field ratio or B_t

$$\Delta_{Te}[\Psi_\mathrm{N}] = 0.047 \cdot a^{-0.59\pm0.28} \langle B_\mathrm{p} \rangle^{-0.73\pm0.23} T_\mathrm{e,ped}^{0.72\pm0.12} n_\mathrm{e,ped}^{0.41\pm0.17} \kappa^{-2.62\pm1.17} \left(\frac{T_\mathrm{e,ped}}{T_\mathrm{i,ped}} \right)^{-0.46\pm0.23} \tag{14}$$

$$\Delta_{ne}[\Psi_\mathrm{N}] = 0.011 \cdot a^{-0.73\pm0.20} \langle B_\mathrm{p} \rangle^{-1.30\pm0.25} T_\mathrm{e,ped}^{0.45\pm0.10} n_\mathrm{e,ped}^{0.65\pm0.16} \kappa^{-1.49\pm0.81} q_\mathrm{cyl}^{-0.42\pm0.17}. \tag{15}$$

In Figure 14 all four regressions are illustrated. The measured pedestal widths show a uniform distribution around the two extended scalings Eq. (14) and (15). The density pedestal width in Figure 14.4 shows an improvement in the description of the AUG data compared to Figure 13.4. The temperature pedestal width in Figure 14.3 shows an overall improvement compared to the dimensionless case which is also visible in the reduction in the RMSE of over 20%. The reason for this difference is the broken coupling between temperature and magnetic field in Eq. (14) contrary to $\beta_\mathrm{p,ped}$ in Eq. (10). This can be illustrated with a an extension of the dimensionless case which then gives the same improved RMSE and alignment with the measurements as does the dimensional description

$$\Delta_{Te}[\Psi_\mathrm{N}] \propto \beta_\mathrm{p,ped}^{0.35\pm0.11} \kappa^{-2.80\pm1.04} T_\mathrm{i,ped}^{0.36\pm0.14} a^{-0.56\pm0.28}. \tag{16}$$

This is essentially the same form as Eq. (14) and illustrates a reduced dependence on poloidal field and pedestal density compared to the dimensionless description in Eq. (10).

When comparing Eq. (10)-(15) with Eq. 6 in Section 3.2 it becomes evident that a significant fraction of the pedestal width variation observed in Ψ_N coordinates will vanish when going to real space coordinates. In Ψ_N coordinates the pedestal width varies more than a factor of 4. In real space coordinates this variation is reduced to roughly a factor of 2.5. This reduction in variation hampers the possibility to apply a regression analysis to this data set. Because the influences of different parameters are too small to be significantly above the uncertainties. A significant fraction of the difference in total variation can be explained with the influence of the shaping factor q_{95}/q_{cyl} on the coordinate transformation Eq. 6. In Figure 15 all discharges with $\beta_{\text{p,ped}}^{0.5} < 0.7$ of AUG, DIII-D and JET align nicely for the temperature width (a) and the density width (b). This suggests the shaping factor caused the separation of the pedestal width for the machines in Figure 12. Figure 15 also illustrates the influence of the machine size. In real space coordinates there is no machine size dependence visible, 95% of the measurements from AUG, DIII-D and JET fall within a 1.0 cm band with a median of 1.7 cm. A correlation of the width in real space with $\beta_{\text{p,ped}}$ is not expected from the theory since the $\beta_{\text{p,ped}}$ dependence is relevant only in Ψ_N coordinates. For example the neutral penetration model [12] would set the pedestal width in real space coordinates. The measurements show no correlation of the density pedestal width with the pedestal top density (Figure 16). However, the neutral penetration is strongly dependent on the parameters in the SOL which vary significantly over the database and were not documented in the database. Therefore, it is not surprising to see a difference compared to experiments which had similar conditions in the SOL and showed a correlation with Δ_{ne} and $n_{\text{e,ped}}$ [8].

6. SUMMARY AND DISCUSSION

In order to obtain reliable information about the width of the edge pedestal it is important to rely not only on high resolution measurements but also on standardized analysis techniques. For multi-machine comparisons in particular, a standardized analysis reduces unnecessary uncertainties. Different methods to characterize the pedestal were benchmarked against each other. The test included the commonly used modified hyperbolic tangent method, the two-line method and a low pass filtering technique. For a series of over 50 independent profiles obtained from discharges with the same conditions the two-line method showed significantly less scatter than the mtanh method. Although, the separatrix position as an additional source for uncertainties is included only in the analysis with the two-line method. Within the uncertainties the absolute values for the pedestal parameters were the same with both methods. In order to test the influence of asymmetries in the profiles, synthetic measurements were constructed with preset pedestal parameters (top, gradient and width). The two-line method is not influenced by asymmetries. The mtanh, however, was also subject to its symmetry and showed changes in the pedestal parameters for a set of simulations with constant pedestal parameters and only varying profile asymmetry. The filter method is reliable only with a priori knowledge about the size of the pedestal. Therefore, it is not useful as a standalone technique, but can, however, be used to supplement other methods. This study found the two-line method best suited for pedestal analysis.

Different boundary conditions in the equilibrium reconstruction can result in deviations of up to 10% of the pedestal width in flux coordinates. Due to diagnostic limits, this is lower than the measurement uncertainty. The deviation was found to depend systematically on the current distribution. This means consistent kinetic equilibrium reconstruction, including measurements of pressure profiles, would be beneficial for profile analysis. Currently the preparation of these equilibria is very time consuming and generally not done iteratively.

In a power scan, the trends of the flux surface compression with global plasma parameters were tested. It revealed that the trend of increasing flux compression with heating power obtained with kinetic reconstructions is reproduced with generic equilibrium reconstructions. Including profile measurements in the reconstruction gives a more detailed, but not entirely different, picture of the equilibrium. The machine size dependence of the flux surface compression at the pedestal, determined with CLISTE for AUG and EFIT for DIII-D and JET, is consistent with a fundamental equilibrium equation. This result provides evidence that there are no systematic deviations between the equilibrium reconstructions for the individual machines. The coordinate system used for examination of the pedestal width is crucial since the coordinate system itself depends on parameters relevant for pedestal width physics, such as pedestal pressure and poloidal magnetic field. In particular, the two dimensionless representations of the pedestal width, Δ_{Ψ_N} and Δ_m/a, are not equivalent. They will scale differently depending on the plasma shape, q_{95}/q_cyl. In the presented database this can account for systematic differences between both coordinates of up to 70%.

The electron temperature and density pedestal width scale similarly with machine size, poloidal field, temperature, density and plasma shape. They depend differently on the temperature ratio, $T_\mathrm{e}/T_\mathrm{i}$, and the magnetic field ratio, q_cyl. The temperature ratio has an impact on the electron temperature pedestal but no influence on the density pedestal width. The magnetic field ratio, or the toroidal field, only has an impact on the density pedestal width and no influence on the temperature width. Different trends for $\Delta_{T\mathrm{e}}$ and $\Delta_{n\mathrm{e}}$ are consistent with previous observations at AUG and DIII-D [7, 8]. Both temperature and density show a strong correlation with the plasma shape, namely the elongation κ for the temperature and κ and q_{95}/q_cyl for the density width. A strong dependence of the density pedestal width with the plasma shape described by the triangularity δ was reported for Alcator C-Mod [41], a δ dependence could not be identified

within the data set examined in this paper.
The dimensionless fits to the database in Ψ_{N} favor scalings with the plasma shape for temperature and density width and $\beta_{\mathrm{p,ped}}^{0.51}$ for $\Delta_{T\mathrm{e}}$ and $\rho_{\mathrm{i}\star}^{0.65}$ for $\Delta_{n\mathrm{e}}$. When transforming Ψ_{N} to r/a coordinates a large part of the shape dependence will be removed from the scaling. This will also result in a reduction of the exponent of the $\beta_{\mathrm{p,ped}}$ dependence of $\Delta_{T\mathrm{e}}[r/a]$ since $\beta_{\mathrm{p,ped}}$ and q_{95}/q_{cyl} are correlated to some extent. The exponent of $\rho_{\mathrm{i}\star}$ in $\Delta_{n\mathrm{e}}[r/a]$ will be relatively unchanged since q_{95}/q_{cyl} appears explicitly in the density width scaling.
Theories in literature which give an explicit prediction for the pedestal width are quite rare. The theory of kinetic ballooning modes predicts a $\beta_{\mathrm{p,ped}}^{0.5}$ dependence of the mean pedestal width $(\Delta_{T\mathrm{e}} + \Delta_{n\mathrm{e}})/2$ in $[\Psi_{\mathrm{N}}]$ [38], which is similar to the $\Delta_{T\mathrm{e}}$ scaling found in the database. The dependence of the normalized gyro radius on the pedestal width is often linked with the theory of turbulence suppression via sheared flows. Depending on mechanisms for turbulence and flow shear the exponent of $\rho_\star$ can vary from 0.5-2.0 [10]. $\mathbf{E}_{\mathrm{r}} \times \mathbf{B}$ flow shear stabilisation would yield $\Delta/a \propto \rho_\star^{0.5} q^{0.5}$ [9]. This mechanism might explain the $\rho_\star$ dependence of the density pedestal width observed in this study. However, the dependence on the safety factor is not reproduced in the measurement. Another theory proposes diamagnetic stabilization of ideal ballooning modes as mechanism to set the pedestal width which would yield $\Delta/a \propto \rho_\star^{2/3}$ [39]. This is consistent with the measurements of the density pedestal width. Neutral penetration [11, 12], which predicts a $1/n_{\mathrm{e}}$ scaling for the pedestal width in real space, could not be tested with the available database. Because the exact fuelling pattern was not known for all discharges and SOL parameters were not included in the analysis. Both play an important role for the process of neutral penetration into the plasma.
To test the capability to extrapolate towards machines of different size the results for an extrapolation towards Alcator C-Mod are given in Table 3. The parameters used for C-Mod in the scaling are $I_{\mathrm{p}} = 0.9$ MA, $B_{\mathrm{t}} = 5.5$ T, $R = 0.67$ m, $a = 0.22$ m, $\kappa = 1.54$, $q_{95} = 3.8$, $p_{\mathrm{ped}} = 35$ kPa, $T_{\mathrm{e,ped}} = 0.4$ keV and $n_{\mathrm{e,ped}} = 27.5 \cdot 10^{19}$ m^{-3} [4] assuming $T_{\mathrm{i}} = T_{\mathrm{e}}$. The pedestal width, calculated with the dimensionless scaling Eq. (10),(11), agrees with the measurements within the uncertainties. The scalings Eq. (14),(15) do not agree with the measurements. In C-Mod $\Delta_{\mathrm{Te}} \simeq \Delta_{\mathrm{ne}}$ which is reproduced for both scalings. The match of the dimensionless scaling towards a machine two times smaller than the analysed ones is encouraging for its use for a machine two times larger. However, the scaling cannot be applied directly since it contains physics parameters which are not known prior to machine operation. Therefore, these parameters ($\rho_{\mathrm{i}\star}$, $\nu_{\mathrm{i}\star}$, $\beta_{\mathrm{p,ped}}$) have to be assumed. This means the following values are not a self consistent prediction, but a check of whether a certain operational point is consistent with the presented scaling or not. This is also the reason why no uncertainties are given for the extrapolated values. For ITER the design values of the engineering parameters are $I_{\mathrm{p}} = 15$ MA, $B_{\mathrm{t}} = 5.3$ T, $R = 6.21$ m, $a = 2.0$ m, $P_{\mathrm{heat}} = 74$ MW, $q_{95} = 3.0$ and $\kappa = 1.8$. The pedestal structure is presumed to be $T_{\mathrm{e,ped}} = 4.0$ keV, $n_{\mathrm{e,ped}} = 7 \cdot 10^{19}$ m^{-3} and $T_{\mathrm{i}} = T_{\mathrm{e}}$. The results for these parameters are listed in Tab. 4. The dimensionless and non dimensionless scalings yield similar results (within 20%) for the ITER pedestal width, this is in contrast to C-Mod. This might suggest that the density dependence is not described accurately in Eq. (14),(15) since this is the only parameter which strongly varies in the extrapolation towards C-Mod, but not towards ITER. However, the impact on the ITER values for the pedestal width should be small, because the density in ITER is very similar to those in AUG, DIII-D and JET. The direction of this deviation could be understood if neutral penetration plays a role in setting the density pedestal width. The density in Alcator C-Mod is 4-10 times larger than those included in the database. Therefore, any effect of neutral penetration would be more pronounced in C-Mod than in the presented data set. In the extrapolation towards ITER the electron temperature pedestal width is about three times larger than the density pedestal width. This is due to the inverse toroidal field dependence and the weaker dependence

on electron temperature in the density width scaling. The temperature pedestal width of $\sim$0.04 in Ψ_{N} is consistent with results of the EPED1.6 code [40]. In order to predict the pedestal top, the width constraint can be combined with peeling-ballooning theory. From the interaction of pressure gradient driven ballooning modes, with current density driven peeling modes one can derive $T_{\mathrm{e,ped}}^{\mathrm{ITER}} \sim 2.5\,\mathrm{keV}$ for $\Delta/a = 0.01$ and $T_{\mathrm{e,ped}}^{\mathrm{ITER}} \sim 6.0\,\mathrm{keV}$ for $\Delta/a = 0.04$ [42]. Within this temperature range the pedestal widths from scalings Eq. (10)-(15) vary by at most 30% from the value for $T_{\mathrm{e,ped}} = 4.0\,\mathrm{keV}$. This means the standard ITER operational point at $T_{\mathrm{e,ped}} = 4.0\,\mathrm{keV}$ and $n_{\mathrm{e,ped}} = 7.0 \cdot 10^{19}\,\mathrm{m}^{-3}$ is consistent with the presented scalings for the pedestal width and peeling-ballooning theory for the pedestal top.

The main results from the analysis of the pedestal width are strong indications of a separation of temperature and density pedestal widths and an important role of the plasma shape. A separation of the width scalings for temperature and density would suggest that the pedestal width is not dominated purely by MHD physics, where both should scale similarly. For mechanisms setting the pedestal width based on transport or atomic physics such a separation is possible. Also, a combination of these processes may be possible. In future studies the impact of different temperature and density edge profiles on the peeling-ballooning instability should be investigated more closely. For example, the bootstrap current density depends differently on the individual profiles of T_{e} and n_{e} [34]. In future machine comparisons a supplementary range of toroidal field, aspect ratio and elongation would help to assess their influence on the pedestal more precisely.

ACKNOWLEDGEMENTS

The authors would like to thank O. Kardaun for his help with statistics questions. This work was supported in part by EURATOM and carried out within the framework of the European Fusion Development Agreement. The views and opinions expressed herein do not necessarily reflect those of the European Commission. This work was supported in part by the U.S. Department of Energy under DE-FC02-04ER54698 and DE-FG02-95ER54309.

REFERENCES

REFERENCES

[1] WAGNER, F. et al., Physical Review Letters **49** (1982) 1408.
[2] SUTTROP, W. et al., Plasma Physics and Controlled Fusion **39** (1997) 2051.
[3] OSBORNE, T. et al., Journal of Nuclear Materials **266-269** (1999) 131.
[4] HUGHES, J. W. et al., Fusion Science and Technology **51** (2007) 317.
[5] URANO, H. et al., Nuclear Fusion **48** (2008) 045008.
[6] GROEBNER, R. J. et al., Nuclear Fusion **49** (2009) 085037.
[7] MAGGI, C. et al., Nuclear Fusion **50** (2010) 025023.
[8] BEURSKENS, M. N. A. et al., Physics of Plasmas **18** (2011) 056120.
[9] ONJUN, T. et al., Physics of Plasmas **9** (2002) 5018.
[10] LEONARD, A. W. et al., Physics of Plasmas **15** (2008) 056114.
[11] WAGNER, F. et al., in *Physics of Plasma-Wall Interactions in Controlled Fusion*, edited by POST, D. E. et al., NATO ASI series: Physics, page 931, 1986.
[12] MAHDAVI, M. A. et al., Physics of Plasmas **10** (2003) 3984.
[13] SNYDER, P. B., Physics of Plasmas **16** (2009) 056118.
[14] KALLENBACH, A. et al., Nuclear Fusion **48** (2008) 085008.
[15] BURCKHART, A. et al., Plasma Physics and Controlled Fusion **52** (2010) 105010.
[16] SALMON, A. N., International Journal of Infrared and Millimeter Waves **15** (1994) 53.
[17] MURMANN, H. et al., Review of Scientific Instruments **63** (1992) 4941.
[18] MLYNEK, A. et al., Review of Scientific Instruments **81** (2010) 033507.
[19] WOLFRUM, E. et al., Review of Scientific Instruments **64** (1993) 2285.
[20] MCCORMICK, K. et al., Fusion Engineering and Design **35** (1997) 125.
[21] FIEDLER, S. et al., Journal of Nuclear Materials **269** (1999) 1279.
[22] SUTTROP, W. et al., IPP Report **I/306** (1997) 1.
[23] FISCHER, R. et al., Fusion Science and Technology **58** (2010) 675.
[24] CARLSTROM, T. N. et al., Review of Scientific Instruments **63** (1992) 4901.
[25] PASQUALOTTO, R. et al., Review of Scientific Instruments **75** (2004) 3891.
[26] RICHARDSON, W. H., Journal of the Optical Society of America **62** (1972) 55.
[27] SCANNELL, R. et al., The Review of scientific instruments **82** (2011) 053501.
[28] GROEBNER, R. J. et al., Physics of Plasmas **5** (1998) 1800.
[29] CHANKIN, A. V. et al., Plasma Physics and Controlled Fusion **48** (2006) 839.
[30] HATAE, T. et al., Plasma Physics and Controlled Fusion **40** (1998) 1073.

[31] MCCARTHY, P. J., Physics of Plasmas **6** (1999) 3554.

[32] LAO, L. L. et al., Nuclear Fusion **25** (1985) 1611.

[33] LAO, L. L. et al., Nuclear Fusion **30** (1990) 1035.

[34] DUNNE, M. G. et al., 38th EPS Conference on Plasma Phys. Strassbourg (2011) P1.070.

[35] SAUTER, O. et al., Physics of Plasmas **6** (1999) 2834.

[36] NEUHAUSER, J. et al., Plasma Physics and Controlled Fusion **44** (2002) 869.

[37] KALLENBACH, A. et al., Nuclear Fusion **43** (2003) 573.

[38] SNYDER, P. B., Nuclear Fusion **49** (2009) 085035.

[39] ROGERS, B. N. et al., Physics of Plasmas **6** (1999) 2797.

[40] SNYDER, P. B. et al., Nuclear Fusion **51** (2011) 103016.

[41] HUGHES, J. W. et al., Physics of Plasmas **9** (2002) 3019.

[42] OSBORNE, T. H. et al., Characteristics of the H-Mode Pedestal and Extrapolation to ITER, in *Proceedings of the 19th IAEA Conference*, pages IAEA–CN–94/CT–3, 2002.

	AUG	*DIII-D*	*JET*	
Nb. data	*69*	*64*	*8*	*141*
I_p *[MA]*	*0.60-1.15*	*0.5-1.5*	*1.7-2.7*	*x5.4*
$\langle B_p \rangle$ *[T]*	*0.18-0.34*	*0.12-0.37*	*0.27-0.40*	*x3.3*
B_t *[T]*	*1.8-2.8*	*0.7-2.1*	*1.8-2.7*	*x4*
$P_{e,ped}$ *[kPa]*	*1.8-9.7*	*0.8-11.8*	*3.2-12.7*	*x16*
a [m]	*0.47-0.51*	*0.52-0.61*	*0.89-0.91*	*x1.9*
R_{mag} *[m]*	*1.70-1.74*	*1.75-1.86*	*3.02-3.09*	*x1.8*
q_{95}	*3.4-7.2*	*2.7-13.4*	*3.4-3.6*	*x5*
q_{95}/q_{cyl}	*1.23-1.45*	*1.11-1.89*	*1.16-1.22*	*x1.7 (8)*
$T_{e,ped}$ *[keV]*	*0.2-0.9*	*0.2-2.1*	*0.5-0.9*	*x10*
$T_{i,ped}$ *[keV]*	*0.3-1.0*	*0.3-1.5*	*-*	*x5*
$n_{e,ped}$ $[10^{-19} m^{-3}]$	*3.7-7.2*	*1.2-6.1*	*3.9-9.3*	*x8*
κ	*1.59-1.74*	*1.69-1.88*	*1.74-1.78*	*x1.2 (1.5)*
δ	*0.21-0.42*	*0.20-0.64*	*0.40-0.43*	*x3*
$\rho_\star$ $[10^{-3}]$	*3.5-6.9*	*5.0-14.3*	*3.7-5.4*	*x4*
$\nu_\star$	*0.30-3.4*	*0.1-0.8*	*0.4-0.9*	*x34*
$\beta_{t,ped}$ $[10^{-3}]$	*2.4-12.0*	*3.7-18.3*	*5.6-15.0*	*x8*
$\beta_{p,ped}$	*0.15-0.54*	*0.21-1.4*	*0.23-0.37*	*x9*

Table 1: Range of key plasma parameters in the database of the three machines AUG, DIII-D and JET. The parameters are defined when they first appear in the text. The last column indicates the range available the parameter spans for the three machines.

Input width [cm]	$\delta\Delta/\Delta[\Psi_N]$	$\delta\Delta/\Delta[R_{maj}]$
1.0	+4 .3 ± 3.3%	− 0.9 ± 1.9%
1.5	+7 .4 ± 3.8%	+0 .4 ± 1.6%
2.5	+10 .1 ± 4.6%	+1.5 ± 1.9%

Table 2: Mean relative broadening for different pedestal widths in Ψ_N and R_{maj} due to use of generic instead of kinetic equilibrium reconstructions. Evaluated for 19 EFIT pairs corresponding to DIII-D discharges.

	Δ_{Te} [Ψ_N]	Δ_{Te} [cm]	Δ_{ne} [Ψ_N]	Δ_{ne} [cm]
dimensionless Eq. (10),(11)	0.053	0.76	0.046	0.66
non dimensionless Eq. (14),(15)	0.12	1.7	0.13	1.9

Table 3: Extrapolation of the pedestal width towards Alcator C-Mod based on scalings derived with AUG, DIII-D and JET. The uncertainty of the extrapolation is about ± 50%. The measured pedestal width for a typical C-Mod discharge is $\Delta\,[\Psi_N] = 0.033 \pm 0.014$ or $\Delta\,[cm] = 0.47 \pm 0.20$ [4].

	Δ_{Te} [Ψ_N]	Δ_{Te} [cm]	Δ_{ne} [Ψ_N]	Δ_{ne} [cm]
dimensionless Eq. (10),(11)	0.036	2.8	0.012	1.0
non dimensionless Eq. (14),(15)	0.045	3.6	0.016	1.3

Table 4: Extrapolation of the pedestal width towards ITER based on scalings derived with AUG, DIII-D and JET.

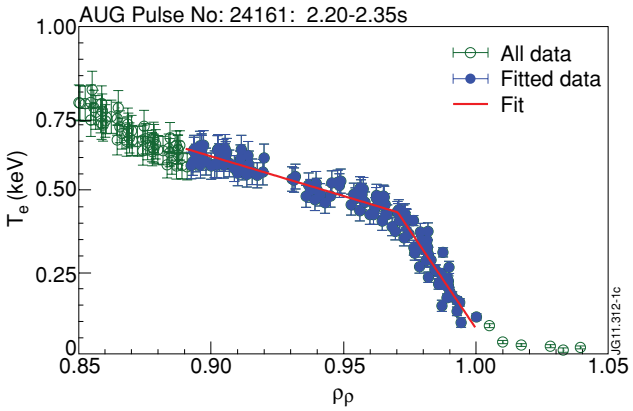

Figure 1: Typical temperature profile (AUG:24161:2.20-2.35s) fitted with Eq. (1) (red, solid).

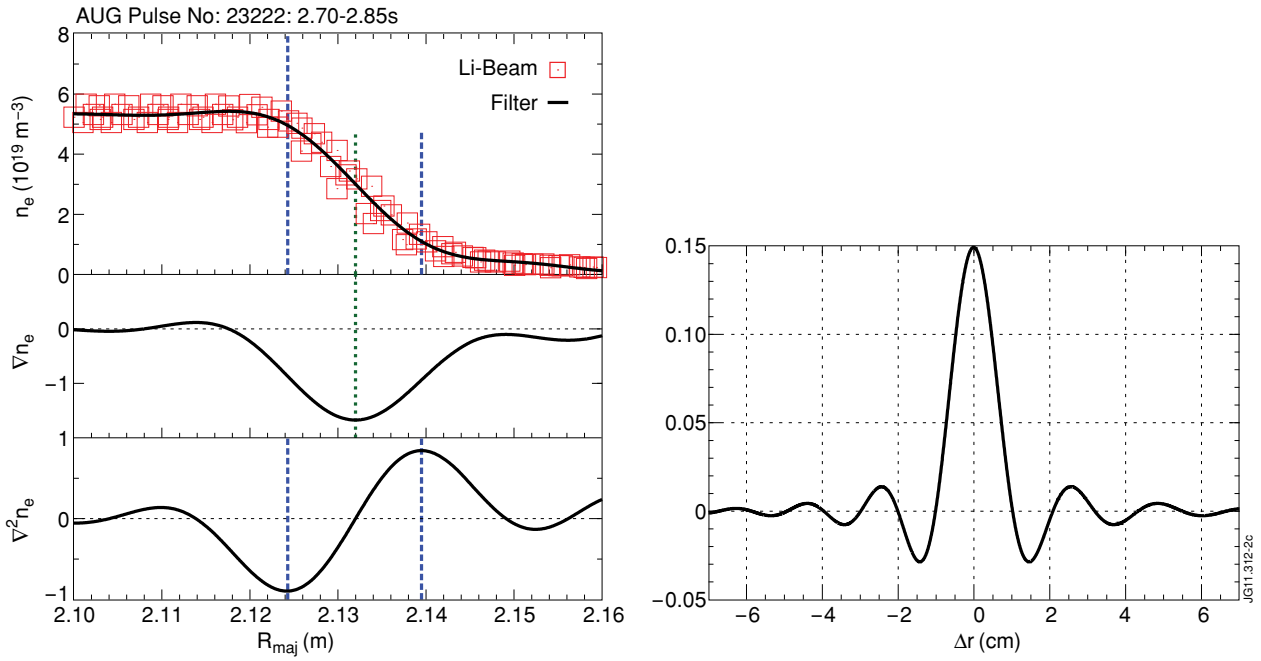

2.1. Examples of data smoothing *2.2. Smoothing kernal in real space*

Figure 2: Left: (top) electron density measurement and smoothed curve, (middle) gradient and (bottom) curvature derived from smoothed curve. The extremas in gradient and curvature are indicated with the dashed vertical lines. Right: Butterworth kernel in real space which was used to generate the smoothed curve.

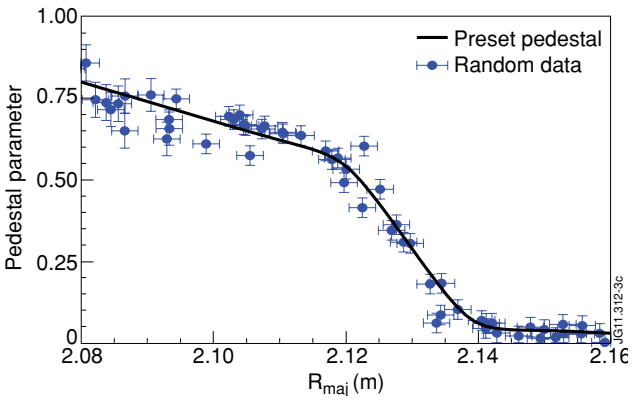

Figure 3: Example for an artificial pedestal profile. The preset pedestal profile is indicated with the solid black line. One set of corresponding random data is indicated with blue circles.

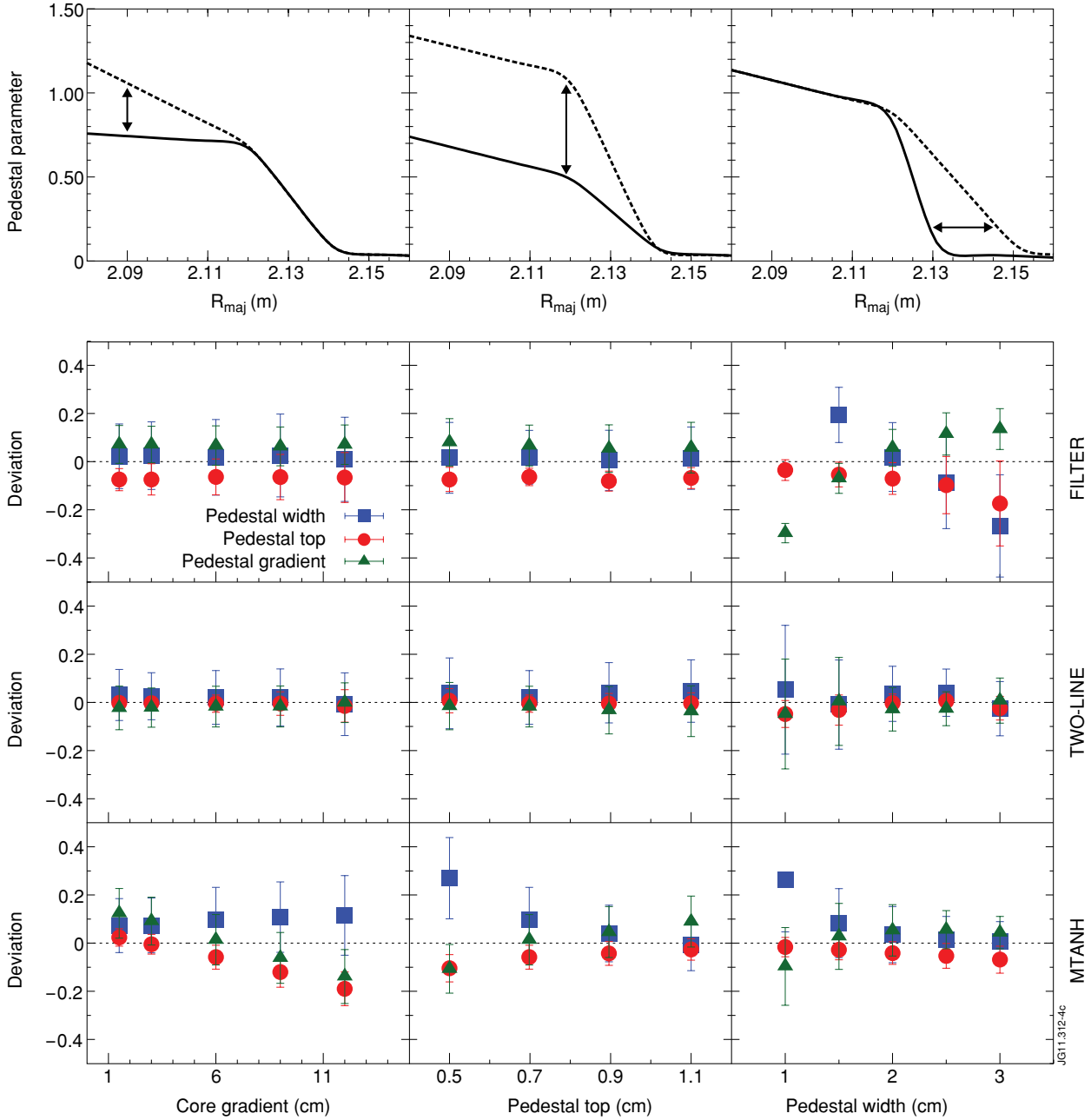

Figure 4: In the top row a sketch illustrates how the pedestal is varied during each simulation. In the lower three rows the results of the pedestal simulation are shown. The relative deviation of mtanh (bottom), two-line (middle) and filter method (top) from preset properties is indicated for the pedestal width (blue, square), the pedestal top (red, circle) and the pedestal gradient (green, triangle). In the left column only the gradient inside of the pedestal top is varied, while the whole pedestal is unchanged. In the middle column pedestal top and gradient are varied, while the pedestal width is unchanged. In the right column pedestal width and gradient are varied, while the pedestal top is unchanged.

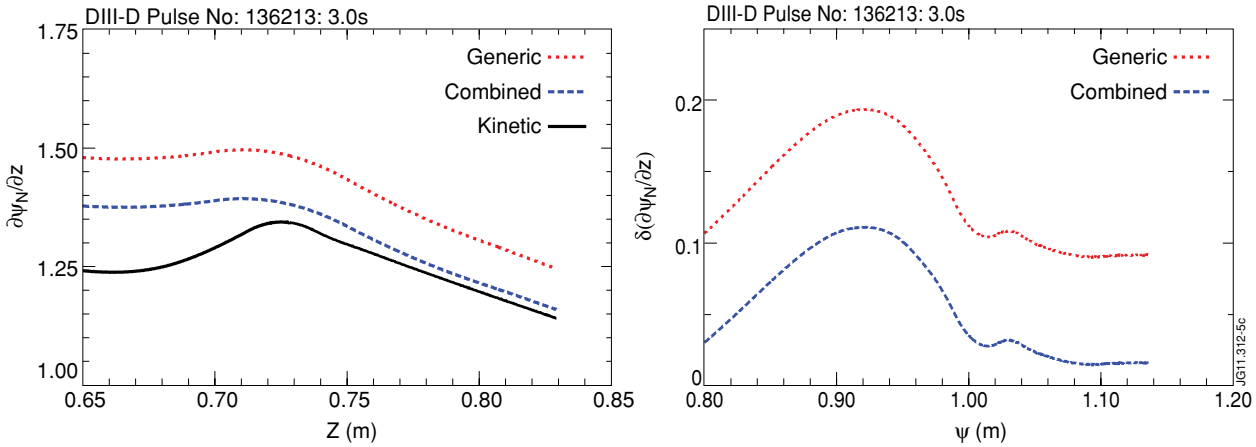

5.1. Absolute values *5.2. Relative deviation from the kinetic profile*

Figure 5: Different results for $\partial\Psi_N/\partial R$ using a generic equilibrium (dotted,red), a kinetic equilibrium (solid,black) or a generic equilibrium combined with the normalization of the kinetic one (dashed,blue). The kinetic equilibrium includes the bootstrap current. The relative deviation is $(\partial\Psi_N/\partial z)/(\partial\Psi_N/\partial z)_{kin} - 1$.

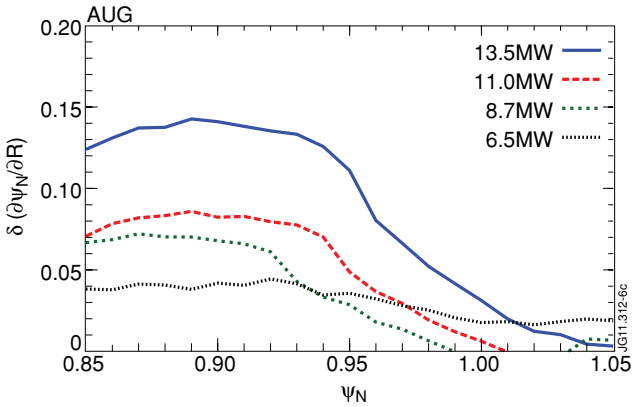

Figure 6: Relative deviation in flux surface compression $\partial\Psi_N/\partial R$ for generic and kinetic equilibrium reconstructions. The generic reconstruction has the larger flux compression. The difference is increasing with heating power. The absolute values are shown in Figure 8. (black: AUG#24167:4.225s, green: AUG#24168:4.225s, red: AUG#22898:4.625s, blue: AUG#23223:5.325s)

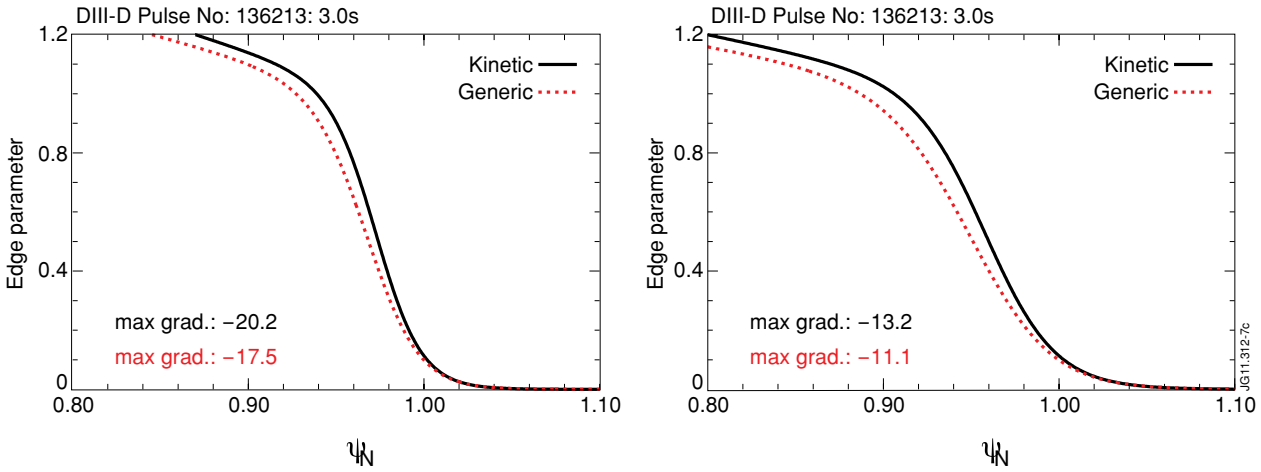

7.1. Initial pedestal width of 1.5cm *7.2. Initial pedestal width of 2.5cm*

Figure 7: The same profile measured in R, z appear differently in flux coordinates depending on the underlying equilibrium reconstruction. The pedestal width becomes larger, the gradient smaller and the profile might be shifted. For comparison the profiles were aligned at the separatrix.

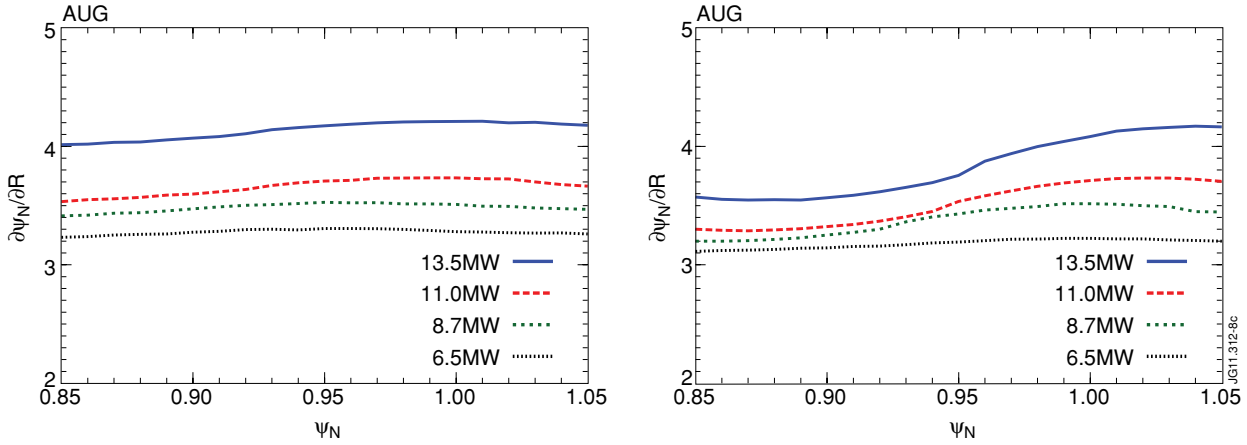

8.1. Generic equilibria *8.2. Kinetic equilibria*

Figure 8: Flux surface compression at the outer midplane for different heating scenarios at ASDEX Upgrade (black: AUG#24167:4.225s, green: AUG#24168:4.225s, red: AUG#22898:4.625s, blue: AUG#23223:5.325s). The generic equilibrium reconstruction with CLISTE (left) shows increasing flux surface compression similar to the kinetic reconstruction (right). The influence of the increased current density due to edge currents becomes visible for the kinetic reconstruction at about $\Psi_N \sim 0.95$.

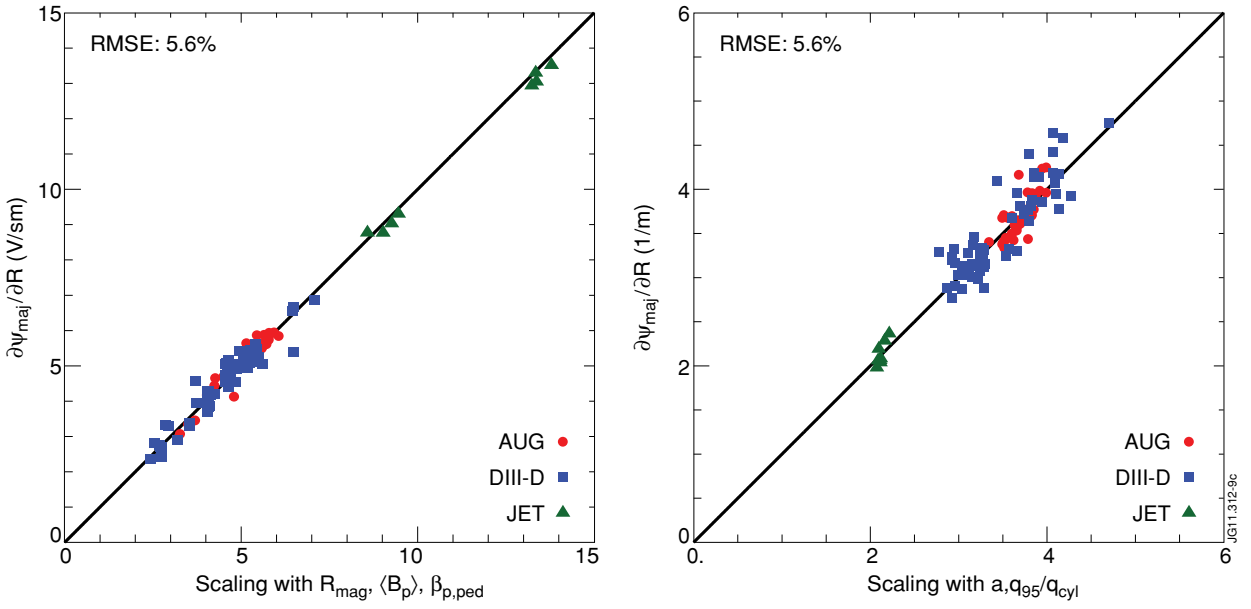

9.1 $12.0 R_{mag}^{1.08} \langle \beta_p \rangle^{1.01} \beta_{p,ped}^{0.14}$ 9.2 $1.65 a^{-0.70} (q_{95}/q_{cyl})^{1.07}$

Figure 9: The flux compression averaged over the last 10% of the plasma radius at the outer midplane is plotted against a best-fit-model. Left for the poloidal flux and right for the normalized poloidal flux. The root mean squared error RMSE was calculated after [9] and is with 5% fairly low in both cases. The subcaptions show the used regression model. For an expression with uncertainties see Eq. (3) and (6).

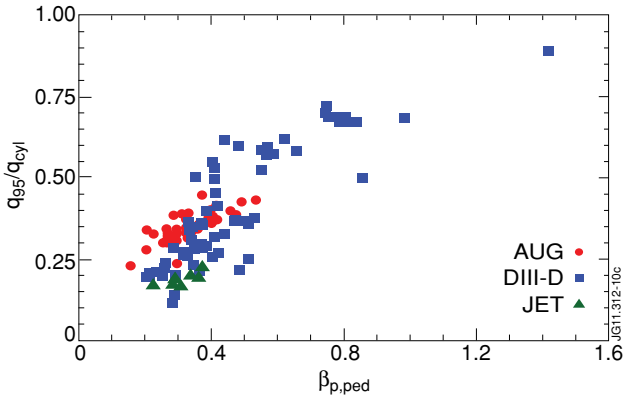

Figure 10: Correlation between the shaping factor $f_q = q_{95}/q_{cyl}$ of Eq. (6) and the poloidal pedestal beta $\beta_{p,ped}$.

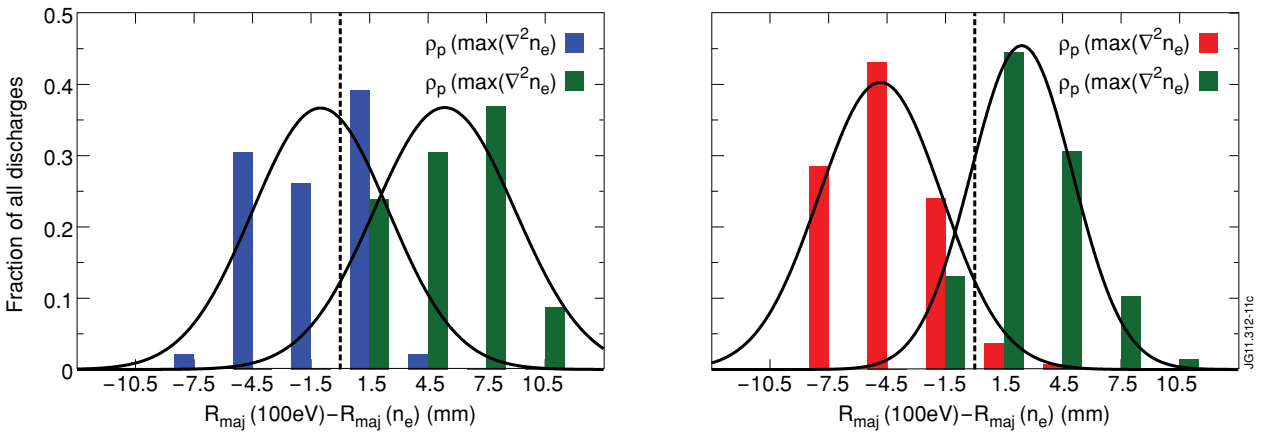

11.1. DIII-D: TS only - T_e and n_e intrinsically aligned *11.2. AUG: ECE, Li-Beam - T_e and n_e not aligned*

Figure 11: Histograms of the difference of positions of T_e =100eV and max($\nabla^2 n_e$) (blue/red) respectively max(∇n_e) (green). The binsize is 3mm and the tics correspond to the middle of each bin. No deviation between positions is indicated with the dashed line. The normal distribution fitted to the histogram is indicated by the solid black line. For DIII-D (left) the position of T_e =100eV matches the one of max($\nabla^2 n_e$) quite well. The AUG (right) data is influenced by a systematic shift of ECE and Li-Beam with respect to each other.

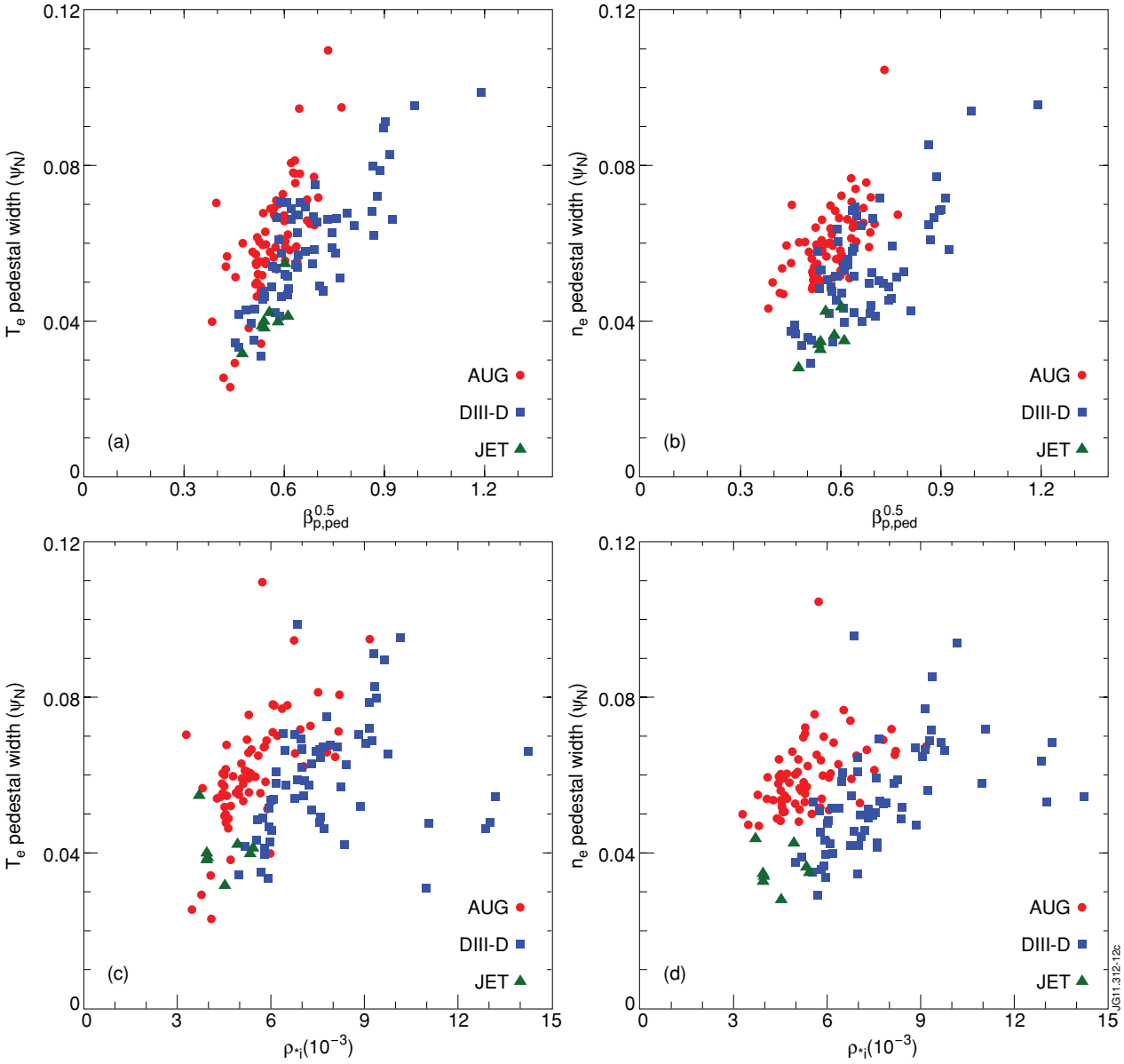

Figure 12: The temperature (left) and density (right) pedestal width of AUG (circle, red), DIII-D (square, blue) and JET (triangle, green) plotted against the square root of the normalized poloidal pedestal pressure (top) and the normalized toroidal gyroradius (bottom).

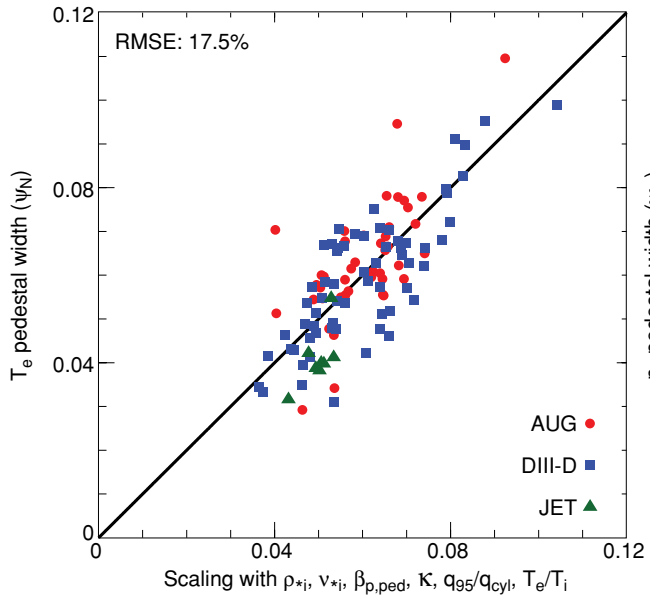

13.1: $0.77 \cdot \rho_{i*}^{-0.01 \pm 0.30}\, \nu_{i*}^{-0.12 \pm 0.10}\, \beta_{p,ped}^{0.49 \pm 0.19}\, \kappa^{-4.03 \pm 1.09}\, (q_{95}/q_{cyl})^{-0.03 \pm 0.59}\, (T_e/T_i)^{0.05 \pm 0.19}$

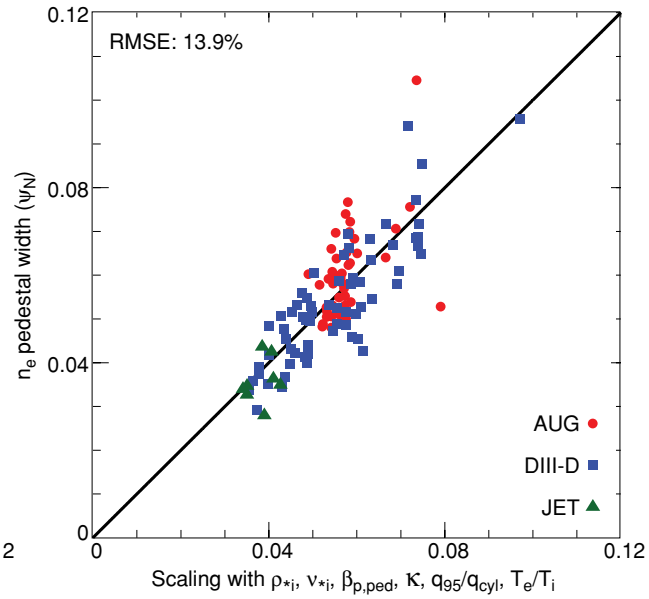

13.2: $3.54 \cdot \rho_{i*}^{0.61 \pm 0.15}\, \nu_{i*}^{0.18 \pm 0.06}\, \beta_{p,ped}^{0.14 \pm 0.15}\, \kappa^{-2.07 \pm 0.83}\, (q_{95}/q_{cyl})^{1.14 \pm 0.43}\, (T_e/T_i)^{0.05 \pm 0.17}$

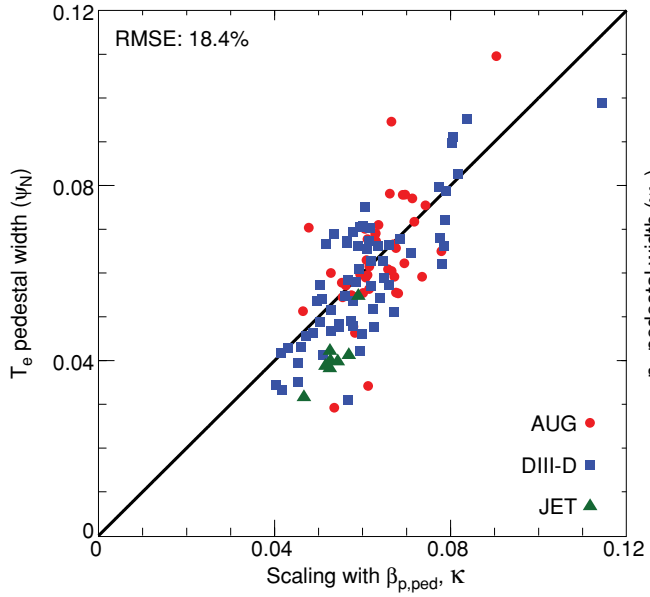

13.3: $0.42 \cdot \beta_{p,ped}^{0.51 \pm 0.09}\, \kappa^{-2.59 \pm 0.85}$

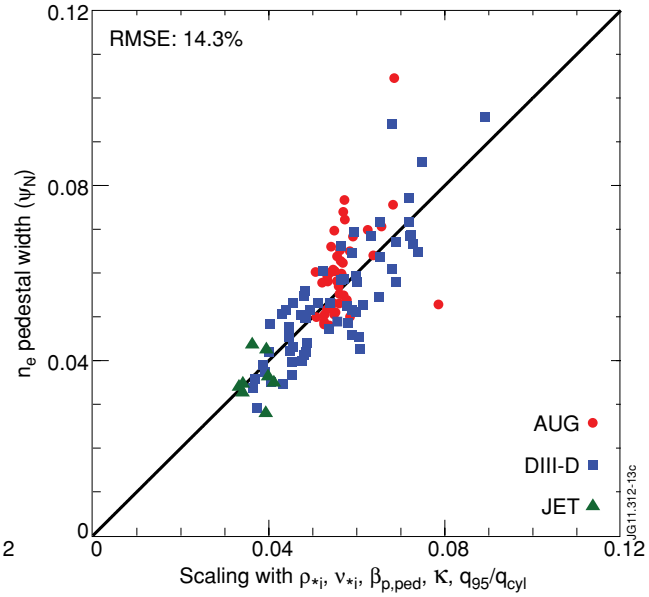

13.4: $2.90 \cdot \rho_{i*}^{0.65 \pm 0.12}\, \nu_{i*}^{0.18 \pm 0.05}\, \kappa^{-1.78 \pm 0.75}\, (q_{95}/q_{cyl})^{1.45 \pm 0.29}$

Figure 13: Log-linear regression applied to temperature (left) and density (right) pedestal width in Ψ_N for AUG (circle, red), DIII-D (square, blue) and JET (triangle, green). In Figure 13.1-13.2 a large number of dimensionless quantities is used in the regression. In Figure 13.3-13.4 the pedestal width is only regressed against the significant quantities.

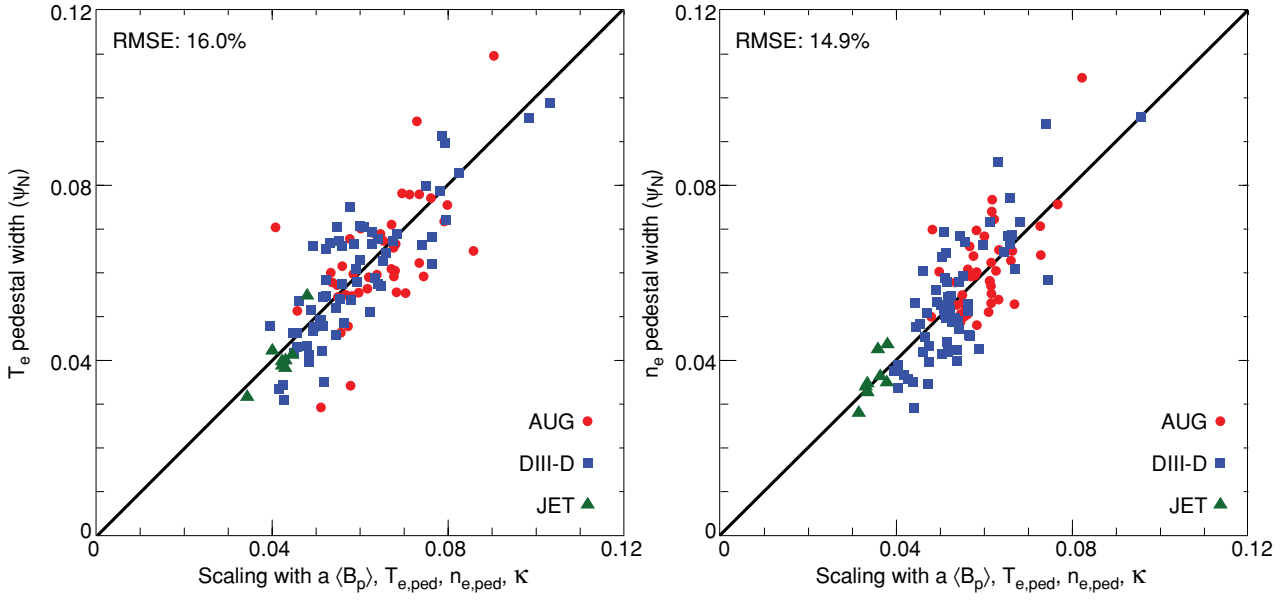

14.1: $0.025 \cdot a^{-0.56} \langle B_p \rangle^{-0.93} T_{e,ped}^{0.62} n_{e,ped}^{0.54} \kappa^{-2.30}$

14.2: $0.011 \cdot a^{-0.67} \langle B_p \rangle^{-1.01} T_{e,ped}^{0.37} n_{e,ped}^{0.51} \kappa^{-1.43}$

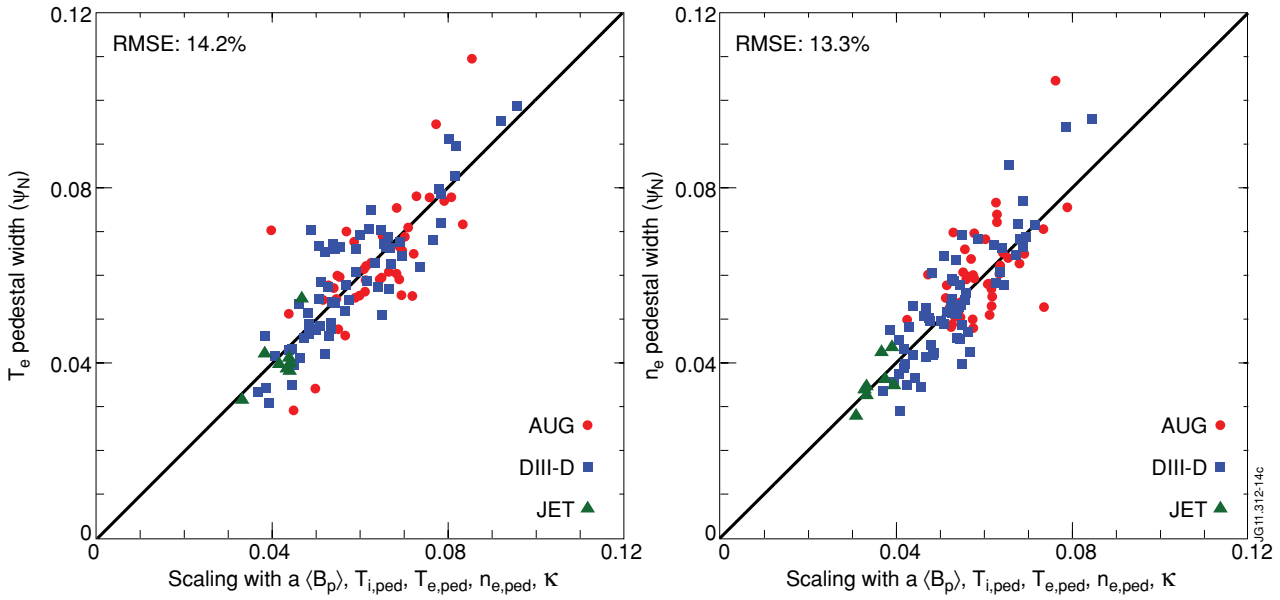

14.3: $0.047 \cdot a^{-0.59} \langle B_p \rangle^{-0.73} T_{e,ped}^{0.72} n_{e,ped}^{0.41} \kappa^{-2.62} (T_{e,ped}/T_{i,ped})^{-0.46}$

14.4: $0.011 \cdot a^{-0.73} \langle B_p \rangle^{-1.30} T_{e,ped}^{0.45} n_{e,ped}^{0.65} \kappa^{-1.49} q_{cyl}^{-0.42}$

Figure 14: Log-linear regression applied to pedestal widths in "N for AUG (circle, red), DIII-D (square, blue) and JET (triangle, green). The temperature pedestal width (left) and density pedestal width (right) is plotted against different regression functions.

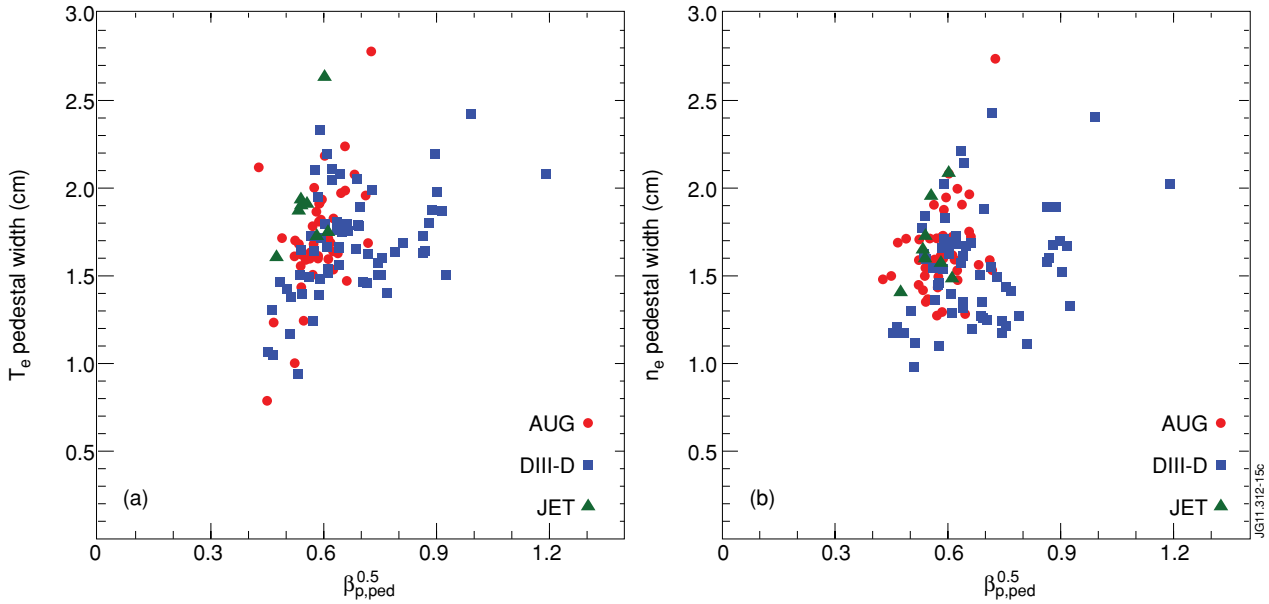

Figure 15: Pedestal width in real space coordinates for the temperature (a) and the density (b) plotted against the normalized poloidal pedestal pressure for AUG (circle, red), DIII-D (square, blue) and JET (triangle, green). This is the equivalent to Figure 12 (a),(b) in real space.

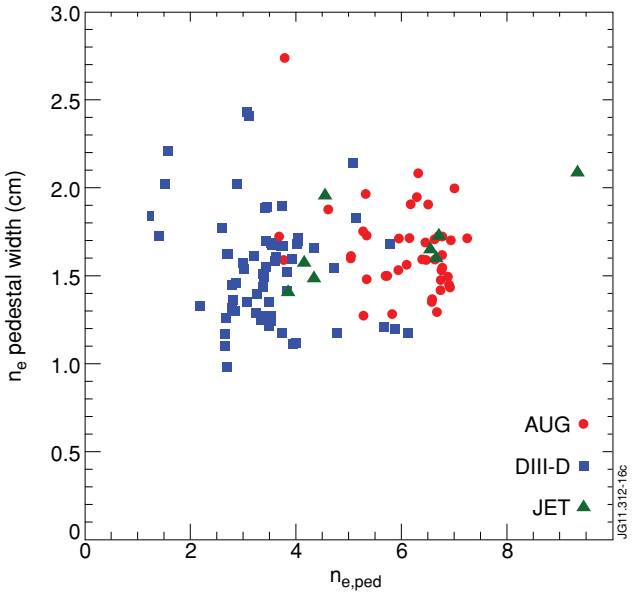

Figure 16: Pedestal width in real space coordinates for the density plotted against the pedestal top density for AUG (circle, red), DIII-D (square, blue) and JET (triangle, green).